Title
A Geodetically Constrained Petrogenetic Model for Evolved Lavas from the January 1997 Fissure Eruption of Kīlauea Volcano

Journal
Journal of Petrology, 65(7)

ISSN
0022-3530

Authors
Scruggs, Melissa A
Spera, Frank J
Rioux, Matt
et al.

Publication Date
2024-07-01

DOI
10.1093/petrology/egae068

OXFORD UNIVERSITY PRESS | Journal of Petrology

Draft Manuscript for Review

A geodetically-constrained petrogenetic model for evolved lavas from the January 1997 fissure eruption of Kilauea Volcano

Journal:	*Journal of Petrology*
Manuscript ID	Draft
Manuscript Type:	Original Manuscript
Date Submitted by the Author:	n/a
Complete List of Authors:	Scruggs, Melissa; University of California Santa Barbara, Department of Earth Science Spera, Frank; University of California Santa Barbara, Department of Earth Science Rioux, Matt; University of California Santa Barbara, Department of Earth Science Bohrson, Wendy; Colorado School of Mines, Department of Earth Science
Keyword:	magma mixing, Episode 54, Kilauea Volcano, Magma Chamber Simulator, Geodesy
Journal of Petrology now offers Virtual Collections of published papers. You may choose up to three collections from the list below. Virtual collections will increase the visibility of your work.:	Thermodynamic Modelling, Oceanic Intraplate Magmatism < Province Themes

A geodetically-constrained petrogenetic model for evolved lavas from the January 1997 fissure eruption of Kilauea Volcano

Melissa A. Scruggs[1], Frank J. Spera[1,2], Matt Rioux[1,3], and Wendy Bohrson[4]
[1]Department of Earth Science, University of California Santa Barbara, 1006 Webb Hall, Santa Barbara, California, 93106-9630. E-mail: TheVolcanoDoc@gmail.com
[2]E-mail: spera@geol.ucsb.edu.
[3]E-mail: mrioux@ucsb.edu.
[4]Department of Geology and Geological Engineering, Colorado School of Mines, 1516 Illinois Street, Golden, Colorado 80401. E-mail: bohrson@mines.edu.

ABSTRACT

Magmatic systems below volcanoes are often dominated by partially crystalline magma over the long term. Rejuvenation of these systems during eruptive events can impact lava composition and eruption style—sometimes resulting in more violent or explosive activity than is often associated with typically low-viscosity volcanic systems. Here, we test whether the geochemical and petrological signatures of low-MgO lavas erupted along the East Rift Zone of Kilauea Volcano on 30-31 January 1997 (Episode 54, Fissures A-F) can be explained by mixing between juvenile basaltic magmas and partially crystalline, rift-stored magma from earlier eruptions. We then compare calculated mixing proportions and petrologically-derived magma volumes to GPS-based geodetic inversions of ground deformation and intrusion growth.

Open-system phase-equilibria thermodynamic models were used to constrain the composition, degree of differentiation, and thermodynamic state of a rift-stored, two pyroxene + plagioclase saturated low-MgO magma body immediately preceding its mixing with high-MgO recharge and degassed drainback (lava lake) magma from Pu'U 'O'o, shortly before disruptive fissure activity within Napau Crater began on 29 January 1997. Mixing models constructed using the Magma Chamber Simulator reproduce the mineralogy and compositions of Episode 54 lavas within uncertainties and suggest that the identity of the low-MgO magma body may be either variably differentiated remnants of un-erupted magmas intruded into Napau Crater in October 1968, or another spatially and compositionally similar magma body. We find the volume of this low-MgO magma body to be ~7.51 Mm^3.

A magma generated by ~23% fractionation of the 1968 intrusion can be mixed with typical 'olivine-control' Kilauean magmas in a 57:43 mass proportion to reproduce the compositions of Fissure A-E lavas. Magmas formed by ~35% fractionation of the 1968 intrusion, when mixed with the same 'olivine-control' Kilauean composition in a 60:40 mass ratio, replicate Fissure F lava compositions. The resultant mineral assemblages and compositions are consistent with the possibility that the now-fractionated, rift-stored magma body was compositionally stratified and ~40-50% crystalline at the time of mixing. Phase-equilibria model results corroborate field and geochemical relationships demonstrating how sub-edificial intrusions at intraplate shield volcanoes can crystallize, evolve, and then be remobilized by new, later batches of mafic magma—and also demonstrate that the pre-eruptive conditions of an intrusive body may be recovered by examining mineral compositions within mixed lavas. Discrepancies between the geodetic constraints on volumes of stored rift versus newly intruded (recharge) magma and our best-fit results produced by MCS mixing models ($m_{mafic}:m_{low\text{-}MgO} \approx 2$ vs. $m_{mafic}:m_{low\text{-}MgO} \approx 0.75$) are interpreted to highlight the complex nature of incomplete mixing on more localized scales as reflected in erupted lavas, compared to geodetically-constrained volumes that likely reflect large spatial scale contributions to a magmatic system. These dissimilar volume relationships may also help to constrain eruptive versus unerupted volumes in magmatic systems undergoing mixing. By demonstrating the usefulness of MCS in modeling past eruptions, we highlight the potential to use it as a tool to aid in petrologic monitoring of ongoing activity.

KEYWORDS

Magma Mixing; Episode 54; Kilauea Volcano; Magma Chamber Simulator; Geodesy

INTRODUCTION

Nearly-continuous eruptive activity at the summit of Kilauea Volcano and along its East Rift Zone (ERZ) has fascinated the public and geoscientists around the world for over four decades. Rapid technological advances of the late 20th and early 21st century—throughout the duration of the 1983-2018 Pu'U 'O'o eruption—provided detailed records of the eruption, making Kilauea one of the best monitored and most intensely studied volcanoes on Earth. This was exemplified from March through April 2018 during the waning stages of the Pu'U 'O'o eruption, as USGS volcanologists were able to accurately forecast the onset of eruptive activity in the Leilani Estates subdivision in time to avoid loss of life (Neal *et al.,* 2019).

The Pu'U 'O'o eruption initiated along the ERZ on 3 Jan 1983, when a dike from Kilauea's summit reservoir intruded into a section of the Middle ERZ and encountered a small body of differentiated, rift-stored magma likely remaining from Kilauea's 1977 eruption (Garcia *et al.,* 1992, 2000). What followed was a series of almost continuous eruptions that would last over 35 years (Neal *et al.,* 2019). Decade-long periods of passive effusion were routinely punctuated by discrete mixing events, where magmas intruded into the ERZ during the Pu'U 'O'o eruption encountered magma in arrested-dike remnants from previous eruptions (Thornber *et al.,* 2003a; Wright & Klein, 2014; Walker *et al.,* 2019), often resulting in the relocation of vents and/or major reorganization of the underlying magmatic system (Orr, 2014). Here, we use individual mixing events as a petrologic tool to track changes in—and components of—

Kilauea's magma storage and transport system, focusing on a series of fissure eruptions that occurred at the end of January 1997, commonly referred to as Episode 54.

GEOLOGIC BACKGROUND

Stretching ~6,000 km over the northern Pacific Ocean, the Hawaiian-Emperor seamount chain preserves an 82-million-year record of Hawaiian mantle plume activity (Clague & Dalrymple, 1987; O'Conner *et al.,* 2013). The northern terminus of the chain, represented by the oldest seamount Meiji, is in the process of being subducted beneath the Aleutian arc (Clague & Dalrymple, 1987; Neall & Trewick, 2008; O'Conner *et al.,* 2013). A slightly southward migration of the Hawaiian hotspot beginning at ~76 Ma, followed by a major shift in the direction of Pacific plate movement to WNW at ~47 Ma, is recorded by the pronounced bend of the Hawaii-Emperor seamount chain (Neall & Trewick, 2008; O'Conner *et al.,* 2013). Magmatism continues at the mantle plume's current location (Ye *et al.*, 2022) as recorded by the Hawaiian Islands and their accompanying seamounts (Neall & Trewick, 2008; O'Conner *et al.,* 2013). The youngest active volcano—Loihi seamount—lies at the southern terminus of the Hawaiian archipelago, and represents the current position of the Hawaiian mantle plume (Clague & Dalrymple, 1987). A thorough recollection of Hawaiian geologic history is provided in Walker (1990) and a bibliography of events occurring prior to 1998 by Wright & Takahashi (1998).

A Detailed Look at the Events Surrounding Episode 54

At 0445 UTC on 30 January 1997 (18:45 HST 29 January 1997), a series of volcanic tremors was accompanied by slippage of the south flank decollement and extension across the ERZ in the vicinity of Napau Crater (Owen *et al.,* 2000; Segall *et al.,* 2001). Within an hour, "a loud whooshing roar" (Harris *et al.,* 1997) accompanied ground deflation measured at both

Makaopuhi Crater and the Kilauea summit—consistent with the removal of magma from those sources—and the disappearance of lava from Pu'U 'O'o crater (Harris *et al.,* 1997; Owen *et al.,* 2000; Thornber *et al.,* 2003a). Geodetic measurements indicate that rift failure initiated a fracture that rapidly grew, filling with magma from storage reservoirs both up- and down-rift (Owen *et al.,* 2000; Segall *et al.,* 2001; Desmarais & Segall 2007). This passive intrusion intersected the ground surface at ~1240 UTC (~2:40 a.m. HST, 30 January 1997), initiating Episode 54, a 22-hour-long fissure eruption up-rift of Pu'U 'O'o, at Napau Crater (Fig. 1b), which ended at 1033 UTC (12:33 a.m. HST, 31 January 1997; Harris *et al.,* 1997). After a 24-day hiatus in activity, a small lava pond appeared within Pu'U 'O'o, signaling that Kilauea's plumbing system was beginning to recover, and marking the start of Episode 55 (Harris *et al.,* 1997; Owen *et al.,* 2000; Thornber *et al.,* 2003a). The lava lake refilled for a period of 32 days, and sporadic outbreaks of lava from the flanks of Pu'U 'O'o began on 28 March 1997 (Garcia *et al.,* 2000; Thornber *et al.,* 2003a; Desmarais & Segall, 2007). Eruptive activity continued, reaching steady-state effusive activity by mid-August 1997 (Garcia *et al.,* 2000; Thornber *et al.,* 2003a).

Episode 54 eruptive products are geochemically distinct from lavas both preceding and following it (Thornber, 2001; Thornber *et al.,* 2003a, 2003b). Episode 53 lavas (22 September 1994 to 30 January 1997) were mafic, averaging ~8.47 wt.% MgO (Fig. 2; Thornber, 2001; Thornber *et al.*, 2003b). Lavas of Episode 54 are unusual in that their compositions became *much* less magnesian over the course of the eruptive sequence, with terminal lavas reaching >51.25 wt.% SiO_2 and <5.75 wt.% MgO (Fig. 2; Thornber, 2001; Thornber *et al.,* 2003a, 2003b). Lavas erupted during early Episode 55 became progressively more and more mafic, peaking at 9.25 wt.% MgO, before settling into steady-state eruptive activity for a decade (Fig. 2; Thornber, 2001; Thornber *et al.,* 2003a, 2003b).

Petrologic and geochemical evidence suggest that the low-wt.% MgO lavas erupted during Episode 54 were a result of mixing between basaltic magmas (e.g., 'olivine controlled') that had been recently supplied to shallow portions of Kilauea's magmatic system and one (or more) previously-intruded, partially solidified dike(s)—referred to here as "rift-stored magmas" (Garcia *et al.,* 2000; Thornber *et al.,* 2003a; Thornber *et al.,* 2015; Walker *et al*., 2019). Considering the likely geometry of the inferred dike complex underlying Kilauea (Walker, 1986; Wallace & Anderson 1998), the location of dikes emplaced in and around Napau Crater (Fig. 1; Thornber *et al*., 2015), and the mixing of distinct magmas during other fissure eruptions along the ERZ (Gansecki *et al*., 2019; Walker *et al*., 2019), dikes intruding into each other appears to be a common occurrence beneath Napau Crater.

THE MAGMA CHAMBER SIMULATOR

Phase-equilibria models constructed in this study were accomplished using the Magma Chamber Simulator (MCS; Bohrson *et al.,* 2014, 2020). MCS is a thermodynamic model for computing phase equilibria, trace element, and isotope systematics in open systems undergoing concurrent or serial fractional crystallization (FC), assimilation of partial melts (A), digestion of stoped blocks (S), and/or magma mixing via magma replenishment/recharge (R). The MCS code, including documentation, examples, and instructional videos are available at http://mcs.geol.ucsb.edu (open access). The phase equilibria engine incorporated within the MCS software used in this study utilizes rhyolite-MELTS (Gualda *et al.,* 2012; Ghiorso & Gualda, 2015). Symbols used in the text for MCS calculations are provided in Table 1.

This study uses the MCS software to determine the source identity and thermodynamic state of the mixing endmembers involved in Episode 54 eruptions. We demonstrate that MCS can be used as a tool to aid in petrologic monitoring of ongoing eruptions by showing its usefulness in modeling past eruptions.

Lavas erupted during Episode 54 were relatively crystal-poor, but were variably clotted with ~3 mm glomerocrysts of ol+pyx+pl (Thornber, 2001), indicating the presence of a multiply-saturated phyric magma, in addition to the near-liquidus 'olivine-control' magmas that typically occupy the Kilauean magma storage and transport system (Thornber *et al.,* 2003a; Orr, 2014; Gansecki *et al.,* 2019). Here, we create phase equilibria-guided mixing models simulating typical 'olivine-control' Kilauean magmas mixing with a more evolved, partially-crystalline, ol+pyx+pl-bearing rift-stored magma, characterizing the onset of Episode 54 (Thornber *et al.,* 2003a). Using MCS, the primary goal of this study is to identify the composition and pre-eruptive thermodynamic state of the stored magma responsible for the presence of evolved melts and disequilibrium glomeroxenocrystic minerals within Episode 54 lavas. This is accomplished by comparing mineral assemblages and compositions *computed* using phase equilibria models to *observed* mineral compositions and assemblages from Episode 54 eruptive products (Thornber, 2001; Thornber *et al.,* 2003a). As our petrogenetic models provide likely compositions and proportions for mixing endmembers as inferred from previous geodetic (Owen *et al.,* 2000; Segall *et al*., 2001; Desmarais & Segall, 2008) and geochemical (Moore & Koyanagi, 1969; Jackson *et al.,* 1975; Thornber *et al.,* 2003a) studies, an equally important goal of this research is to establish if a self-consistent petrogenetic model of Episode 54 is also consistent with geodetically-constrained volume displacements initially determined by Owen *et al.* (2000), and further refined by Segall *et al*. (2001) and Desmarais & Segall (2007).

VOLUME ESTIMATES OF EPISODE 54 ENDMEMBER MAGMAS

The events surrounding Episode 54 were captured in detail by a continuous Global Positioning System (GPS) network previously installed on Kilauea volcano (Owen *et al.,* 2000; Segall *et al.*, 2001; Desmarais & Segall, 2007). Seismic tremors occurred for ~8 hours preceding eruption onset, accompanied by drainback of Pu'U 'O'o's lava lake, deflation of the Kilauea summit caldera, and seismic activity underneath Makaopuhi Crater—indicating the movement of magma at these three areas (Owen *et al.*, 2000; Thornber *et al.*, 2003a). During this time, extension within the southeastern flank of Kilauea's edifice enabled a passive intrusion to form in a weakened area of the ERZ beneath Napau Crater (Owen *et al.,* 2000; Thornber *et al.,* 2003a). By the conclusion of this eruptive episode, the geodetic constraints suggest approximately 23 Mm^3 of magma had accumulated beneath Napau Crater, forming a roughly planar body that extended 5.15 km in length, 1.96 m in width, and ~2.24 km in the vertical extent (dipping so that the base of the intrusion was at ~2.4 km depth; see also Plate 2 in Owen *et al.,* 2000).

Point-source "Mogi-style" models developed by Owen *et al.,* (2000) and Segall *et al.,* (2001) suggest the Episode 54 intrusion was sourced from three known reservoirs: (1) 1.50 Mm^3 of magma from the Kilauea Summit reservoir; (2) 1.20 Mm^3 of magma from a reservoir underlying Makaopuhi Crater; and (3) 12.7 Mm^3 of magma representing drainback from the Pu'U 'O'o lava lake. Dike volume estimates require the presence of an additional magma of unknown volume (Owen *et al.*, 2000) that geochemical studies suggest may be a cooler, multiply-saturated (ol+cpx+plag) magma, previously intruded into and stored within the rift zone (Garcia *et al*., 2000; Thornber *et al.*, 2003a). This geodetic model was further refined by Desmarais & Segall (2007), who later provided revised estimates of intrusion along strike and down-dip lengths to 5.3 km and 2.7 km, respectively, with an additional 0.08 m of post-intrusion opening towards the base of the dike and transient deformation continuing for several months following the Episode 54 eruption. These estimates coincide with the findings of Segall *et al.,* (2001), who demonstrate that two-thirds of the final dike volume had been intruded at the time of eruption, and that further volume accumulation continued after Episode 54, albeit at a much lower rate. From these geodetic estimates, we calculate that the volume of the intrusion at the time of the Episode 54 eruption was 22.91 Mm^3, and that the total final volume of the intrusion was 29.49 Mm^3, in good agreement with transient deformation models (Segall *et al.,* 2001; Desmarais & Segall, 2007). We calculate the maximum volume of rift-stored magmas beneath Napau Crater – Owen *et al.*'s unknown fourth component – to be ~7.51 Mm^3 by volume closure. The parameters obtained from the literature and the results of our volume calculations are presented in Table 2. For purposes of internal consistency, volumes quoted above are given to two decimal places with uncertainties on the same order of magnitude as those estimated by Owen *et al.* (2000). For the petrogenetic modeling, however, relative volumes are more important than absolute values.

CONSTRUCTION OF THE MIXED MAFIC ENDMEMBER (MME) MAGMA

The geodetic (Owen *et al.,* 2000; Segall *et al.,* 2001; Desmarais & Segall 2008) and petrologic (Garcia *et al.,* 2000; Thornber, 2001; Thornber *et al.*, 2003a) data support a magma mixing model for the Episode 54 lavas wherein an arrested and partially crystallized intrusive body (rift stored magma) interacted with distinct batches of mafic magma from the Kilauea Summit reservoir, a reservoir below Makaopuhi Crater, and drain-back from the lava lake at Pu'U 'O'o. For our petrogenetic modeling, we used published geochemical data—as detailed below—to estimate the major oxide composition of these three magma sources and then combined them to create a single "Mixed Mafic Endmember" (MME) composition (Table 4; green star in Fig. 4) in proportions constrained by the aforementioned geodetic relations. This MME is our best estimate of the mafic endmember involved in the mixing events interpreted to have occurred during Episode 54.

As magmas from Kilauea's summit reservoir are reasonably homogenized prior to their arrival and subsequent eruption at the East Rift Zone (Edmonds *et al.,* 2015), we used the average steady-state composition of Episode 53 lavas erupted from Pu'U 'O'o (Thornber *et al.,* 2003a) to represent the Kilauea summit component of the MME. Magmas derived from underneath Makaopuhi Crater were represented by a pumice—similar in composition to the Kilauea Summit component—from the 1968 Makaopuhi Crater eruption (Wright *et al.,* 1968). Finally, the largest ingredient (~83%) in the MME comes from magmas present in the Pu'U 'O'o conduit & underlying reservoir (Harris *et al.,* 1997; Owen *et al.,* 2000; Thornber *et al.,* 2003a) immediately preceding the onset of Episode 54, modeled using the last-erupted bulk lava sample from Episode 53 (KE53-1844; Thornber *et al.,* 2003b). Using these compositions and proportions constrained by geodetic measurements (see Table 2), the MME composition was generated by bulk mixing and renormalized to 100 wt.% (Table 4). Fractional crystallization (FC) of the MME composition was modeled using MCS, where FeO/FeO_{tot} was initially set at a value corresponding to fO_2 = QFM-0.5, and phase equilibria models were run at P = 0.05 GPa and 0.5 wt.% H_2O_i without restricting fO_2 along a buffer (Supp. Item B). Despite some uncertainty in the exact compositions and volumes of the different MME components, the MME composition is dominated by the large volume drain-back from Pu'U 'O'o'—suggested by geodetic measurements to provide the largest volume of melt (Owen *et al.,* 2000)—*and* the compositions of the three components of the MME are relatively similar (Wright *et al.,* 1968;

Thornber *et al.,* 2003a, 2003b). Although our MME is not drastically different from the mafic endmember proposed by Thornber *et al*. (2003a), by adopting these compositional and geodetic constraints we directly link our petrologic models to magmatic volumes.

IDENTIFICATION OF THE MORE EVOLVED, RIFT-STORED ENDMEMBER

Prior to the Episode 54 eruption, Kilauea Volcano steadily effused near-liquidus, ol-bearing, high (~8.47 wt.%) MgO basaltic lavas for almost a decade (Thornber *et al.,* 2003a, 2003b). Episode 54 lavas are markedly different from those lavas erupted either before or after 30-31 January 1997: the more evolved lavas (avg. MgO = 6.38 wt.%; Fig. 2) erupted from Fissures A-E contain complexly zoned phenocrysts and microphenocrysts of ol, cpx, and pl, occurring either as individual crystals or as glomerocrysts containing <80% interstitial glass; Fissure F lavas are petrographically similar to Fissure A-E lavas, but are even less magnesian (avg. MgO = 5.8 wt.%; Fig. 2) and bear orthopyroxene (opx)—either as scarce, reversely-zoned crystals or as exsolution lamellae within augite (Thornber, 2001; Thornber *et al.,* 2003a).

Although disagreement about the identity of the more evolved magmas required to produce Episode 54 bulk rock and mineral compositions (Garcia *et al.,* 2000; Thornber *et al.,* 2003a; Walker *et al*., 2019) is still prevalent, there is consensus that mixing of more typical, mafic Kilauean magmas (olivine-control; our MME) with a less magnesian, multiply-saturated magma *must* have occurred. The complex mixing history preserved in Episode 54 eruptive products was extensively documented by Thornber *et al.* (2003a), who suggested that a "phenocryst-laden" (Thornber *et al*., 2003a) and evolved magma body was rapidly reheated by and mixed with lower viscosity, higher-*T* mafic magmas, then erupted over a limited range of temperatures. Thornber *et al.* (2003a) found that this evolved, rift-stored mixing component was derived from nearly 40% fractionation of a bulk composition *equivalent* to an opx-bearing lava erupted from the Lower East Rift Zone in 1955. Given that no opx-bearing lavas have erupted in Napau Crater, they suggested that an equivalent composition might be derived from magmas intruded into the Napau Crater region during 1963, 1968, or 1983 (Garcia *et al.*, 2000; Thornber *et al.*, 2003a; Walker *et al.*, 2019). Conversely, Garcia *et al.* (2000) and Walker *et al.* (2019) maintain that two different bulk compositions—that existed at the time as discrete, molten magma bodies located beneath Napau Crater—are responsible for the anomalous compositions of Episode 54 lavas. Specifically, Walker *et al.* (2019) argues that leftover melts from the initial 1983 intrusion are the low-MgO mixing component that produced Fissure A-E lavas, and that Fissure F lavas show no evidence of magma mixing and are *themselves* the erupted portion of a discrete rift-stored, low-MgO magma body. This study tests these various hypotheses by constructing a series of phase-equilibria models to compare model results to measured Episode 54 lava and mineral compositions, with the goal of discerning between the different proposed low-MgO endmember compositions.

After reviewing available literature and examining fissure locations in and around Napau Crater (Fig. 1; Thornber *et al.,* 2003a; Thornber *et al.,* 2015; Walker *et al.*, 2019), we identified five potential candidates for the arrested dike composition: a tholeiitic basalt (K63-2) erupted from fissures within Napau Crater during October 1963 (Moore & Koyanagi, 1969); N68-4 and N68-8, erupted in October 1968 (Jackson *et al.,* 1975); and KE1-1 and KE1-49, erupted at the very beginning of the Pu'U 'O'o eruption (Thornber *et al.,* 2003a, 2003b). The 1955 opx-bearing composition (TLW 67-34 from Wright & Fiske, 1971) was not tested as a potential endmember because it (yellow polygon in Fig. 4)–or any potential liquids derived from this composition–are too deficient in wt.% Al_2O_3 to serve as a mixing endmember to produce Ep54 lavas; further the

1955 eruption took place >20 km downrift from Napau Crater (yellow polygon in Fig. 1a inset; Wright & Fiske, 1971).

To constrain potential compositions of the evolved dike at the time of mixing, and therefore determine whether they might represent the evolved mixing endmember during the Episode 54 eruption, we first used MCS to model the evolution of dike liquids as they fractionally crystallize (ornamented dashed lines in Fig. 4, see also Supp. Figure B1). Lavas erupted from Fissures A-E and Fissure F are compositionally distinct (Figs. 2 & 4), suggesting that the mafic endmember mixed with two different compositions—one more evolved (Fissure F) than the other (Fissures A-E)—as represented by the dashed green mixing lines (l^{mix}) in Figure 4. Compositions of ol, pyx, and pl from Episode 54 glomerocrysts are best reproduced by fractionation of a magma with an initial bulk composition equivalent to N68-4 (Supp. Fig. B2, see also Supp. Item B). This composition is more similar to lavas erupted from Kilauea Volcano during periods of steady-state activity than most of the other dikes examined, implying that N68-4 is likely more representative of the initial bulk composition of the dike at the time of its emplacement than other considered compositions (Table 4). Consequently, dike N68-4 was selected as the best reference LLD (liquid line of descent) for construction of the more evolved, rift-stored endmember.

To estimate the extent to which N68-4 had fractionated by the time Episode 54 occurred (i.e., fractionation between 1968 and 1997), we constructed two different mixing lines (l^{mix}) by calculating a regression line between the MME composition (green star) and the average composition of lavas from Fissures A-E (AE^{avg} in Table 4; Thornber *et al.,* 2003a) and another between the MME and the Fissure F average composition (F^{avg} in Table 4; Thornber *et al.,* 2003a). Each l^{mix} was then projected to its intersection with the modeled N68-4 LLD (represented by blue asterisks in Fig. 4) produced by fractionation of the rift-stored magma body. When comparing wt.% MgO vs. wt.% Al_2O_3 for the data set, the geochemical variations depicted in Figure 4 (see also Supp. Figure B1 for the full suite of bivariate diagrams) illustrate the orthogonal relationships between any modeled LLD and each of the calculated l^{mix} regression lines. Hence for any LLD, there should exist two different melt compositions that can serve as the low-MgO mixing endmembers for the Fissure A–E versus Fissure F eruptions (Langmuir *et al.,* 1978).

The intersection between each l^{mix} and the LLD in MgO-Al_2O_3 space was used to determine an initial estimate of the wt.% MgO of the low-MgO mixing endmember magmas required to produce the lava compositions and mineral assemblages of both $A\text{-}E^{avg}$ and F^{avg} (i.e., how fractionated the rift-stored dike was at the time of mixing). The l^{mix} for $A\text{-}E^{avg}$ intersects N68-4's LLD at ~5.1 wt.% MgO, and the l^{mix} for F^{avg} intersects at ~3.5 wt.% MgO, as represented by the vertical blue lines in Figure 4. Ideally, each l^{mix} would intersect the LLD for every major element at the same wt.% MgO, but in reality, this is not the case; the intersection between the l^{mix} and the LLD fall at slightly different wt. % MgO for each element. At no point along the LLD for any modeled dike composition does there appear to be a single composition that could be used as an evolved endmember to match all elements for either $A\text{-}E^{avg}$ or F^{avg}. This is likely due to the analytical uncertainties in the original analyses of the dike compositions, the geologic uncertainties in the model (e.g., f_{O2}, wt.% initial H_2O, P; purple color fields in Fig. 4), and inherent uncertainties within the phase-equilibria models (pale yellow color fields in Fig. 4), which we have quantified in Supp. Item A and illustrated in Figures 4 and 5.

Given the model uncertainty (purple and pale-yellow color fields in Fig. 4; see also Supp. Item A) we adjusted the mixing endmember compositions predicted by the intersection between the l^{mix} and LLDs to values that satisfy *both* the linearity requirements of bulk mixing (Langmuir *et al.,* 1978) and lie within calculated uncertainty of the modeled LLD. These adjusted compositions could then be used as the low-MgO endmembers for our Episode 54 mixing models. In selecting mixing endmembers and proportions, we exercised the constraint that the entire rock composition (i.e., *all* oxides) must reflect identical proportions of the identified endmembers (Langmuir *et al.,* 1978; von Engelhardt, 1989). We therefore defined two best-fit fractionated rift stored magma endmember compositions—one falling on the l^{mix} for $A\text{-}E^{avg}$, and the other falling on the l^{mix} for F^{avg}—by using the LLD as a reference point for least squares regression. At any given MgO, the intersection between the l^{mix} and the LLD predicts a concentration for each major oxide. For the Fissure A–E and Fissure F rift stored magma endmembers, we adjusted wt.% MgO to find a single value, where the predicted concentrations for each major element along the l^{mix} line at the chosen wt. % MgO plots as close as possible to the intersection between l^{mix} and the LLD produced by fractionation of N68-4 (i.e., we minimized the sum of the residuals between that predicted major oxide concentration along l^{mix} and the intersection of l^{mix} and the LLD). This was done twice—first by minimizing the squared residual of wt.% MgO, and second by minimizing the sum of squared residuals for all oxides. The singular data point along l^{mix} that satisfies both these requirements is considered to be the most likely low-MgO endmember responsible for forming the hybrid compositions. For each l^{mix}, concentrations of major oxides other than wt.% MgO were then fixed as that oxide's l^{mix} value corresponding to the selected wt.% MgO (Figure 4; Supp. Fig. 1). The above method results in a 5.28 wt.% MgO composition as the low-MgO rift-stored magma needed to reproduce $A\text{-}E^{avg}$, and a 4.43 wt.% MgO composition as the low-MgO rift-stored magma needed to reproduce F^{avg}; complete bulk magma compositions for both low-MgO endmembers are given in Table 5, and illustrated in Figure 5. Initial volatile contents of the low-MgO endmember magma were constrained by exploratory models (Supp. Item A) and ultimately set at 0.5 wt.% H_2O and 0.02 wt.% CO_2 (Table 5). Small variations in these values created had little to no discernable differences in the results presented here.

The "best fit" MgO content of 4.43 wt. % for fractionated endmember for the Fissure F lavas is significantly higher than the ~3.5 wt. % MgO value noted above, based only on the intersection between lmix and the LLD in MgO versus Al_2O_3 space. However, the higher MgO is consistent with the paucity of Fe-Ti oxides in Episode 54 lavas (Thornber *et al*., 2003a), as the N68-4 models reach ilmenite saturation around 4.5 wt.% MgO. Although it *is* possible that any ilmenite crystals were completely reabsorbed, the short duration of Episode 54 (<24 hrs; Harris *et al.,* 1997; Owen *et al.,* 2000) and preserved disequilibrium nature of the erupted mineral assemblage imply otherwise. We instead consider it likely that the evolved endmembers must have had $\gtrsim$ 4.5 wt.% MgO, which is consistent with our best fit model.

Using the least squares method, we find that the stored magma body responsible for the evolved nature of Episode 54 lavas (Table 5) was derived from ~23% (Fissures A–E) to ~35% (Fissure F) fractionation of an intruded magma *very* similar in composition to sample N68-4 (Jackson *et al.,* 1975)—a basalt collected from the October 1968 fissure eruption and associated intrusion at Napau Crater. The low H_2O contents of mafic Kilauean lavas (Wallace & Anderson, 1998), coupled with the high vesicularity of Episode 54 lavas, suggest the presence of an exsolved fluid phase within the low-MgO endmember, consistent with significant fractionation. We emphasize that although the regressed endmember compositions do not fall exactly on the LLD for dike N68-4 (Fig. 5), they are within (or close to within) estimated geologic and phase-equilibria uncertainties (Supp. Item A; with the exception of MnO and P_2O_5), and that the selected MgO—and therefore degree of fractionation—is constrained by the orthogonal relationship between the LLD and the l^{mix} required by the MME and the composition of the erupted lavas from Fissures A–E and Fissure F.

PHASE-EQUILIBRIA MAGMA MIXING MODEL: METHODS AND RESULTS

After determining the best-fit endmember compositions needed to reproduce $A\text{-}E^{avg}$ and F^{avg}, we conducted two series of numerical experiments to constrain the relative proportions of liquid and crystals of the rift-stored magma at the time of the Episode 54 mixing event. This model envisions a two-step process, where an intrusion with a composition similar to N68-4 intruded and fractionated along the LLD as described in the previous section, with all solid products being removed from the system (this stage involves the 23-35% fractional crystallization, as outlined above). In a second stage described herein, the crystal-free, now-fractionated melt continues to cool and crystallize in-situ prior to the Episode 54 eruption. The crystal cargo of this now-fractionated magma was not removed prior to its mixing with the MME, and therefore impacts the thermodynamics of the mixing event. We model this second stage as a closed-system process, wherein the rift-stored low-MgO magmas are modeled as bulk compositions of liquid + crystals that mix with the MME melt composition. For both the Fissure A–E and Fissure F low-MgO endmembers, equilibrium crystallization of each residual (fractionated) liquid composition was modeled over the range of T correlating with crystal contents from 20-80% (φ=20-80). A resulting mushy, low-MgO endmember was then mixed with the near-liquidus (φ<1) MME; mixing proportions required to reproduce $A\text{-}E^{avg}$ and F^{avg} (Table 4; Thornber *et al.,* 2003a) were determined by linear combination, and are given in Table 5 along with other input parameters for each numerical experiment. Full MCS results, supplemental figures, and individual MCS output files are provided in Supp. Item C.

The resultant bulk hybridized magma compositions (Fig. 5) are required to overlap the average Episode 54 lava compositions by the method we used to determine the rift-stored endmember and mixing proportions. The MCS models are useful because mineral compositions in equilibrium with the hybrid lavas produced in the Recharge + Fractional Crystallization (RFC) models can be compared with observed mineral compositions from erupted Episode 54 lavas to estimate the crystallinity of the low-MgO magma at the time of the mixing event. Thornber (2001) and Thornber *et al.* (2003a) report that Episode 54 lavas are highly vesiculated and relatively aphyric, containing <5 vol.% phenocrysts of ol, pl, cpx, and rare cpx+pl glomerocrysts. Thornber *et al.* (2003a) also report that groundmass crystallinity of Episode 54 lavas varies considerably, with glass making up anywhere between ~1 and ~80 vol.% of the matrix. Additionally, Fissure F lavas contain both rare opx phenocrysts and high-Mg# opx lamellae within cpx phenocrysts, requiring that the low-MgO endmember for Fissure F was two-pyx saturated.

We note that the petrographic descriptions of Garcia *et al*. (2000) greatly differ from those of Thornber *et al*. (2003a). In particular, Garcia *et al.* (2000) report only very rare ol and pl phenocrysts in their Episode 54 lavas, with rare microphenocrysts of ol + pl + cpx; no glomerocrysts, cpx phenocrysts, or opx are reported. This discrepancy in reported mineral assemblages may be due to inadequate sampling, as only a single sample from each Episode 54 fissure was reported by Garcia *et al*. (2000), whereas Thornber (2001) and Thornber *et al.* (2003a) examined a total of 29 samples from Episode 54. Furthermore, the ol + pl + cpx + opx mineral assemblage is depicted in backscattered electron images of Episode 54 lavas (Thornber *et al*., 2003a). We therefore attempt to reproduce the more evolved mineral assemblage reported by Thornber *et al.* (2003a) in our phase-equilibria models. Mineral compositions computed in our mixing models are presented in Figure 6 and discussed in detail below; full results of our mixing models are provided in Supp. Item C.

DISCUSSION

Previous studies have addressed the issue of magma mixing in the petrogenesis of Episode 54 eruptive products (Garcia *et al.,* 2000; Thornber *et al.,* 2003a; Walker *et al*., 2019). In addition to reexamining the mixing processes responsible for Episode 54 lava compositions, the current study incorporates revised geodetic constraints, considers measured lava effusion rates, and adds a phase-equilibria perspective to the volcanologic picture. Indeed, the advantage of a phase-equilibria study lies in the ability to compare more than just bulk rock geochemistry—modal abundance of phases and their compositions can be evaluated as well to obtain a more complete view. Here we review the petrologic constraints on the low-MgO endmember based on the mineralogy and phase compositions of Episode 54 lavas, and discuss how these results—combined with our MCS modeling—constrain the composition and pre-eruptive state of the rift-stored magma body.

Determining the Minerology and Crystallinity of the Shallow, Rift-Stored Magma Body

Decreasing specific enthalpies dictate the mineral phases and compositions that will be thermodynamically stable as the low-MgO endmember becomes more crystalline (Table 6). Therefore, we can use mineral compositions produced in the MCS forward models to constrain the pre-eruptive state of the low-MgO rift-stored magmas. Although we utilize a thermodynamic model (MCS; Bohrson *et al*., 2020) to model a dynamic process (the rapid mixing of different magma batches), we are effectively examining the equilibrated, pre-mixing state of the endmember magmas—rendering MCS an appropriate diagnostic tool.

State of the Rift-Stored Low-MgO Endmember as constrained by Fissure A-E forward models

The results of the MCS forward models combined with major element trends demonstrate that mixing between our MME and a bulk composition produced by ~23% fractionation of a basalt similar to one intruded into the Napau crater region in 1968 (N68-4; Jackson *et al.,* 1975) generates a low-MgO endmember magma that reproduces the mineral assemblages and compositions present in lavas erupted from Fissures A-E. Our model predicts a mixing proportion of 57% low-MgO component and 43% MME. Here we look in detail at how model mineral compositions for the mixed lavas can be compared to the observed phenocryst compositions in the Episode 54 lavas to constrain the degree of crystallinity of the rift-stored magma immediately preceding the Episode 54 mixing event.

Fissure A-E lavas are triply-saturated, containing ol, cpx, and pl (Fig. 6, see also Thornber *et al.,* 2003a). Ol is a stable hybrid phase in the MCS models when the low-MgO endmember is <70% crystalline, and is replaced by pigeonite (low-Ca pyroxene) when the crystallinity of the low-MgO endmember increases to 80%, whereas augite remains a stable phase in all MCS models. As depicted in Figure 6, there are two populations of Fissure A-E ol: a) higher Fo phenocrysts and microphenocrysts in equilibrium with the different mafic magmas sourced for the Episode 54 intrusion (dark gray circles), and b) lower Fo microphenocrysts and syn-eruptive skeletal crystals and epitaxial overgrowths crystallized from the hybrid lavas (lighter gray circles; Thornber, 2001; Thornber *et al.,* 2003a). Similarly, higher-An pl in equilibrium with lavas more mafic than those erupted during Episode 54 (dark gray circles in Fig. 6) were found alongside those with lower An which crystallized from hybrid melts (intermediate gray circles in Fig. 6; Thornber *et al.,* 2003a). At low-MgO endmember crystallinities up to 50%, our MCS model results reproduce ol and augite compositions in equilibrium with hybrid melts; this relationship is shown on Figure 6 in the compositional overlap between low to moderate-crystallinity MCS results (red to yellow squares) and the intermediate gray circles interpreted to represent crystals in equilibrium with the hybrid magma erupted at fissures A-E. For those phase-equilibria models where the low-MgO endmember is ≥40% crystalline, MCS-produced pl compositions overlap a subset of the measured plagioclase interpreted to be in equilibrium with the hybrid magma (intermediate gray circles). Figure 6 shows that while compositional overlap is evident between the measured and modeled plagioclase, calculated T estimates of crystallization are higher for measured crystals (based on geothermometry found in Thornber *et al.,* 2003a) than are predicted in our forward models. This disparity may reflect uncertainty in the geothermometry estimates (Thornber *et al.,* 2003b), the MCS forward models (Supp. Item A), and the intrinsic disequilibrium nature of a rapid mixing event, which cannot be accurately represented by phase-equilibria modeling. For the rift-stored magma body, an upper limit of 50% crystallinity is supported by the absence of Fe-Ti oxides or opx in Fissure A-E lavas (Thornber *et al.,* 2003a); Fe-Ti oxides are produced as stable MCS hybrid phases for those models where the low-MgO endmember is ≥60% crystalline, and opx is stable in the low-MgO endmember if it is ≥50% crystalline. The lack of these phases in erupted Fissure A-E lavas could be due to sampling bias, and so the trace amounts of opx in the modeled low-MgO endmember at φ=50% are geologically plausible. disequilibrium textures and mineral compositions may not necessarily be reflected in the results of an equilibrium MCS model.

Finally, we can also use the compositions of phases that crystallize from the low-MgO endmember in the MCS models prior to mixing to further constrain the magma's thermodynamic state immediately preceding the mixing event. Potentially antecrystic cpx recovered from Fissure A-E lavas (light gray circles in Fig. 6; Thornber *et al.,* 2003a) can be reproduced by equilibrium crystallization of the low-MgO endmember (diamonds in Fig. 6) over a range of ~1094-1056˚C (Fig. 6), correlating with φ = 20-50%. Further, measured pl from Fissure A-E lavas (gray circles) form a linear trend from An_{61} to An_{81}, where the low An grains (light gray circles) may be antecrysts from the rift-stored magma, and the highest An grains (dark gray circles) are likely antecrysts from the mafic recharge magmas (Fig. 6; Thornber *et al.,* 2003a). Equilibrium crystallization of the low-MgO endmember at T=1069˚C (φ=50) reproduces An_{61} pl, although estimates of crystallization *T* (light gray circles) are higher than our MCS model results (Fig. 6). These additional constraints reinforce our finding that prior to 29 January 1997, the rift-stored magma body was a magmatic mush consisting of 40-50% crystals.

State of the Rift-Stored Low-MgO Endmember as constrained by Fissure F forward models

Results of the MCS forward models demonstrate that a bulk composition produced by ~35% fractionation of N68-4 (Jackson *et al.,* 1975) can generate a low-MgO endmember magma that reasonably reproduces the mineral assemblages and compositions present in Fissure F lavas when mixed with the MME. In this case, the hybrid magma is ~60% low-MgO endmember component and ~40% mafic endmember component. Mineral compositions produced in the MCS forward models further constrain the state of the evolved intrusion that mixed to form Fissure F lavas, and suggest that this low-MgO endmember was ~40% crystalline immediately preceding the Episode 54 mixing event.

Like the lavas that preceded them, Fissure F lavas are triply-saturated, bearing equilibrium ol, cpx, and pl (Fig. 6). Ol is a stable hybrid phase in the MCS models when the low-MgO endmember is ≤50% crystalline at the time of mixing, pigeonite is present in hybrid lavas for those MCS models where the low-MgO endmember is 40-70% crystalline, and opx can only be produced in MCS as a hybrid phase when the low-MgO endmember is >70% crystalline (Fig. 6, Table 6). Ol with $>Fo_{80}$ are sourced from mafic recharge magmas (dark gray circles; Thornber *et al.,* 2003b), and so we do not expect them to be equilibrium phases in model hybrid lavas. The least fayalitic ol measured in Fissure F lavas (lighter gray circles, $\sim Fo_{72}$), which are interpreted to be in equilibrium with the hybrid magma, can be recreated in our lower-crystallinity (φ=20-30) MCS models (Fig. 6). Both opx and cpx compositions produced in the Fissure F mixing models (squares) have lower Mg# than measured pyroxenes from hybrid Episode 54 lavas (gray circles; Thornber *et al.,* 2003a), and we address these compositional disparities later in this section. MCS-produced pl compositions overlap with measured Fissure F pl compositions (gray circles) when the low-MgO endmember in our MCS models is 30-70% crystalline (Figure 6); however, geothermometry estimates of crystallization *T* (Thornber *et al.,* 2003a) for pl present in Fissure F lavas are higher than those produced in our MCS models (Fig. 6), likely reflecting the same caveats that we discussed above for the Fissure A–E models. Although Fe-Ti oxides are not present in Episode 54 lavas, they appear as hybrid phases in our MCS models, increasing from <2 vol.% when the low-MgO endmember is 40% crystalline to ~16 vol.% at the maximum modeled crystallinity (φ=80). As myriad factors contribute to the saturation of a phase in rhyolite-MELTS, we consider the minor amounts (<2 vol.%) of oxides to most likely reflect model uncertainties.

As with Fissure A-E lavas, we place additional constraints upon the thermodynamic state of the rift-stored magma body tapped to produce Fissure F lavas by comparing the compositions of modeled phases in equilibrium with the Fissure F low-MgO endmember to measured antecryst compositions in the erupted lavas (light gray circles). Equilibrium crystallization of the low-

MgO endmember produces a mineral assemblage of augite + pigeonite + pl at T≥1076˚C (corresponding with φ≤30); at T=1067-1036˚C (φ=40-60), pigeonite is replaced by opx, but returns at T≤1012˚C (φ≥70). Opx lamellae are present within some Fissure F cpx crystals, and a lone opx xenocryst was reported in Fissure F lavas by Thornber *et al.* (2003a). Although none of the forward models produce either opx or pigeonite with high Mg# comparable to those present in measured lavas (gray circles), the forward models *do* produce opx as an equilibrium hybrid phase when the low-MgO endmember is ~80% crystalline (Fig. 6). More likely, however, is that the observed orthopyroxene originates from the low-MgO magma, as orthopyroxene is a stable phase in the modeled low-MgO endmember over a range of T=1067-1036˚C, corresponding to φ=40-60% (Fig. 6). Our best estimate of the state of the low-MgO endmember required to reproduce F^{avg} at the time of mixing is therefore φ ≈ 40, where opx is a stable phase in the low-MgO endmember at the time of mixing, and the observed common mineral assemblage of ol + cpx + pl is stable in modeled hybrid lavas.

The Mg# of ferromagnesian phases produced in our MCS models is systematically lower than those measured in Fissure F lavas. Extensive exploratory modeling (Supp. Item A) was done to select the best intensive parameters for our initial phase-equilibria models (P=0.5 kbar and f_{O2}=QFM-0.2). As our MCS runs are a bifurcated process, modeling of magma mixing could be done at lower pressures (P=0.1 kbar) under more oxidized conditions (f_{O2}=QFM) to represent crystallization of a dike at shallow depth. Although running our mixing models at lower *P* increases pyroxene Mg# (Putirka, 2008; see also Supp. Item C), *P*=0.1 kbar is the lowest-possible *P* for which our models would return a result. Adjustment of f_{O2} to more oxidized conditions would also increase pyroxene Mg# (Appendix A), but f_{O2}=QFM is near the upper limit of oxidation for Kilauean lavas (Carmichael 1991). We also point to our FC results for

K63-2 (Fig. 4; Supp. Fig. B1), which has a bulk composition similar to N68-4, but a measured ferrous-ferric ratio equivalent to QFM+0.2 (Table 4). The oxidized nature of the starting bulk composition results in a liquid line of descent much more enriched in Al_2O_3, and produces significantly larger quantities of lower-Mg pyx and lower-An pl when compared to measured Ep54 mineral compositions (Supp. Fig. B2), suggesting the observed offset in the composition of Fe-Mg phases is not related to fO_2. Given the model and geologic limitations, we put more weight on reproducing the Fissure F mineral assemblage (as described above) than attempting to match mineral compositions exactly.

The differences in the low-MgO endmembers for the Fissures A–E and Fissure F lavas may reflect the geometry of the eruption and differences in magma density. Fissure F is ~2.25 km up-rift of Fissure E, and at a higher elevation (~53 m elevation difference; see Fig. 1 & Sherrod *et al.*, 2021). Calculated bulk rock densities (Table 7) of the hypothetical low-MgO endmember compositions show that, at P=0.1 kbar, the Fissure F low-MgO endmember magma (~35% fractionated from the original dike composition) is more buoyant than the less-evolved Fissure A-E low-MgO endmember (~23% fractionated), regardless of magma crystallinity. This is consistent with the Fissures A–E and Fissure F low-MgO endmembers being derived from a compositionally-stratified, differentiating arrested dike. Fissure eruptions from feeder dikes have been shown to propagate laterally as an eruption progresses (Geshi *et al.,* 2020); lateral propagation of mafic recharge magmas interacting with an already emplaced, compositionally zoned and partially crystalline dike to form the final intrusive volume (Figure 7; see also Animation 1) may explain why the final fissure of the eruptive sequence opened up-rift, and why its lavas were more evolved than the lavas erupted down-rift from Fissures A-E.

Linking Petrology with Geodesy – an integrated hypothesis for Episode 54

A key goal of this study was to determine if a relationship can be established between syn-eruptive geodetic measurements and the geochemistry of lavas associated with the observed deformation. The timing, volume, location, and degree/direction of ground deformation for Kilauea Volcano's Episode 54 eruption is well-documented (Harris *et al.,* 1997; Owen *et al.,* 2000; Desmarais & Segall, 2007). The detailed eruption narrative of Episode 54, when paired with updated seismic and geodetic constraints and a detailed geochemical and petrological time-series of samples, affords a useful opportunity to link the eruption chronology and geochemical compositions to magma volumes estimated by two distinct methods, petrologic modeling and geodesy.

A revised volume estimate of the rift-stored low-MgO magma body

The results of our petrologic mixing models suggest that the erupted Episode 54 lavas are a mixture of 57-60% rift-stored intrusion and 43-40% residential mafic magmas. Following the same method as Thornber *et al*. (2003a)—that ~60% of the 0.3 Mm^3 of erupted lavas are low-MgO component—we find the syneruptive volume of the rift-stored, multiply-saturated 1968 intrusion to be ~0.18 Mm^3. However, early Episode 55 lavas erupted before 1 August 1997 also contain antecrysts derived from this low-MgO magma body, so this volume estimate is an absolute minimum.

Our calculated volume for Owen's unknown fourth component is 7.51 Mm^3, but solely using a geodetic approach precludes identification of a magma composition (Segall, 2019). The 'missing' 7.51 Mm^3 may be the underlying ERZ conduit, represent a single low-MgO endmember magma body involved in the Episode 54 mixing event, or it may represent any number of unerupted intrusions stored beneath the rift zone (Walker, 1986; Garcia *et al.*, 2000;

Thornber *et al.*, 2003a; Walker *et al.*, 2019). Following the method of Thornber *et al.* (2003a) and using their same recharge rate of 0.3 Mm^3/day for the few weeks following Episode 54, if Thornber *et al*.'s proposed volume of 7.3 Mm^3 *was* indeed the ERZ conduit volume underlying Napau Crater, the volume closure estimate for the crystalline and evolved low-MgO magma body would be ~0.21 Mm^3—a volume just slightly larger than indicated by our petrologic mixing models. This may seem a reasonable result, but it does not allow for the necessary volumes of low-MgO magma that were erupted during early Episode 55 (Supp. Item D). Bulk major oxide compositions and disequilibrium antecrysts within lavas erupted from Pu'U 'O'o between 28 March 1997 and 1 August 1997 contain variable proportions of the Episode 54 low-MgO component (Fig. 2; see also Thornber *et al.*, 2003a and 2003b), indicating that mafic recharge magmas flushed out any remaining rift-stored low-MgO magmas (Thornber *et al.*, 2003a; Helz *et al.*, 2014) during this five-month period. Further, a *drastic* drop in the proportion of low-MgO component in erupted lavas occurred after 1 August 1997, when transient movement (i.e., opening) of the rift zone ended (Fig. 3; see also Supp. Item D). That larger amounts of the low-MgO magma body continued to be incorporated into erupted lavas *until rift expansion ceased* would imply that the body of low-MgO magma was likely entirely flushed out during refilling of the rift system, and not by the ~7.3 Mm^3 of magma that had accumulated as of 24 February 1997. We therefore reason that the 7.51 Mm^3 of magma does, in fact, represent the volume of the low-MgO magma body involved in the Episode 54 mixing event (and subsequent recovery), and not the volume of the underlying ERZ conduit.

Reconciling Geodetically-Determined Intrusion Volumes with Petrologic Modeling Results

MCS models suggest that lavas erupted from Fissures A-E formed as a mixture between a near-liquidus mafic magma derived from multiple sources within the Kilauean edifice (MME, Table

5), and a variably fractionated and compositionally stratified arrested dike that erupted from fissure openings in Napau Crater. The MCS models also suggest that the mafic magma interacted and mixed with a more evolved part of the same arrested dike to produce Fissure F lavas, but with a slightly greater mixing proportion of the low-MgO endmember.

AE^{avg} (Table 4; Thornber *et al.,* 2003a) is a mixture of 57% low-MgO magma ($f_{low\text{-}MgO}$ = 0.57 ±0.01)—derived by ~23% fractionation (Table 5) of an initial composition similar to N68-4 (Tables 4-5; Jackson *et al.,* 1975)—and 43% mafic magmas (MME, Table 5) derived from multiple sources within the Kilauean edifice ($m^{mafic}:m^{low\text{-}MgO} \approx 0.75$; Table 5). F^{avg} (Table 4; Thornber *et al.,* 2003a) can be matched by a mixture of 60% low-MgO magma ($f_{low\text{-}MgO}$ = 0.60 ±0.005)—derived by ~35% fractionation ($m^{mafic}:m^{low\text{-}MgO} \approx 0.67$; Table 5) of an initial composition similar to N68-4 (Tables 4-5; Jackson *et al.,* 1975)—and 43% mafic magmas (MME, Table 5).

Our phase equilibria-guided model results are inconsistent with our volume closure calculations based on the geodetic data. Our volume closure calculations based on the point-source "Mogi-style" models by Owen *et al.,* (2000) and Segall *et al.,* (2001), indicate that 15.4 Mm^3 of mafic magma mixed with a maximum of 7.51 Mm^3 of low-MgO, rift-stored magma body, yielding a mixing ratio of $m^{mafic}:m^{low\text{-}MgO} \approx 2$. This ratio is consistent with the conclusions of Thornber *et al.* (2003a). We interpret the differences in these model results as providing insight into how localized mixing events are documented in the rock record, highlighting how magma mixing is more often than not a heterogeneous process. Our modeling suggests slightly different mixing proportions for Fissures A–E versus Fissure F, and geochemical trends also make the different parageneses between erupted lavas quite apparent (Figs. 5-6); these results are consistent with the different eruption locations for Fissures A-E and Fissure F and underscore the complexity of the dike/rift system at Kilauea. Indeed, for magma batches to mix and homogenize to completion within a 22-hour time period (Harris *et al.,* 1997) would be unexpected. The low vol. % of phenocrysts and glomerocrysts reported by Thornber (2001) and Thornber *et al.,* (2003a), when considered alongside the large volumes of magmas required by geodetic models and low volumes of lava erupted during Episode 54, suggest that the entire volume of the 1968 intrusion was likely not erupted.

CONCLUSIONS AND IMPLICATIONS

The April 2018 conclusion of Kilauea Volcano's ~35 year-long Pu'U 'O'o eruption presents an opportunity for holistic, retrospective studies. After initial eruption onset, activity was characterized by periods of steady-state effusion, interrupted sporadically by intrusions into weakened areas of the ERZ (Thornber *et al.,* 2015; Walker *et al*., 2019), sometimes resulting in brief fissure eruptions that produced low-MgO lavas choked with glomerocrystic crystal clots derived from more evolved, rift-stored magma bodies (Orr *et al.,* 2015; Thornber *et al.,* 2015). With each new intrusion, the underground storage and transport system of Kilauea changed (Thornber 2001; Thornber *et al.,* 2003a; Orr 2014; Orr *et al.,* 2015; Gansecki *et al.,* 2019). The results of our study demonstrate that whole rock and mineral chemistries coupled with thermodynamically-constrained geochemical modeling, can provide new insight into mixing processes, the identity and physical state of rift stored bodies during mixing events, and the relative mixing proportions of mafic and rift-stored magmas that combine to erupt hybrid (*sensu lato*) lavas.

Lavas erupted from Episode 54 fissures are basaltic and relatively aphyric, containing <5% phenocrysts and glomerocrystic clots of cpx + pl (Thornber *et al.,* 2003a), and have much lower MgO contents than lavas erupted before 30 January 1997 (Fig. 2). In agreement with previous research (Garcia *et al.,* 2000; Thornber *et al.,* 2003a), we conclude that a previously emplaced, evolved intrusion below Napau Crater mixed with mafic magmas from Kilauea Summit, Makaopuhi Crater and mafic drainback from the Pu'U 'O'o reservoir, to form the low-MgO basalts erupted during Episode 54. Our findings differ from those of Garcia *et al.* (2000) and Thornber *et al.* (2003a) in that we find that magmas derived from a single, compositionally stratified magma body that was intruded into Napau Crater in 1968 (N68-4; Jackson *et al.,* 1975) can mix with mafic Kilauea magmas to reproduce average Episode 54 bulk lava, mineralogy and mineral compositions, without necessitating the interaction of multiple, low-MgO rift-stored magma bodies to produce Episode 54 lava compositions. Further, by constructing phase equilibria-based mixing models of Episode 54, we can better define the pre-eruptive state of the magmatic system. In contrast to the suggestion that the low-MgO intrusions were pure liquids at the time of mixing (Walker *et al.*, 2019), we find that the portion of the intrusion-derived magma needed to produce lavas erupted from Fissures A-E was ~23% fractionated from the initial bulk composition, and 40-50% crystalline at the time of mixing. We also conclude that a stratigraphically-higher (and more evolved) region of the remnant 1968 intrusion located underneath the western edge of Napau Crater and sampled by the Fissure F eruptions, was produced by ~35% fractionation of the initial intrusion, and was 40-50% crystalline at the time of eruption. These results are inconsistent with the hypothesis of Walker *et al.* (2019) that the Fissure F lavas represent an unmixed low-MgO endmember composition. The mafic component mixed with the two, now compositionally distinct but petrogenetically-related, low-MgO endmembers in proportions of $m^{mafic}:m^{low\text{-}MgO} \approx 0.75$ and $m^{mafic}:m^{low\text{-}MgO} \approx 0.67$ to produce Fissures A-E and Fissure F lavas, respectively. We also find that the proportions of the individual magma sources, as constrained by geodetic measurements, can be used as a guide to construct mixing endmembers, but directly linking geodetic volume estimates to magma chemistry is complicated by complex mixing processes that occur rapidly prior to eruption, and a direct link between the total volume of a magma body and its geochemistry is likely complicated by incomplete mixing that occurs over short distances and timescales. This novel application of the Magma Chamber Simulator could be widely employed at other volcanic systems where the conditions of a partially-crystalline magma are in question, and may prove useful for future studies of volcanic hazards.

CRediT AUTHORSHIP CONTRIBUTION STATEMENT

This project was conceptualized by Wendy Bohrson and Frank Spera, and designed by Melissa Scruggs and Frank Spera. Model refinement, investigation of the research question, and formal analysis of model results was conducted by Melissa Scruggs, with supervising contributions and guidance from Frank Spera, Matt Rioux, and Roberta Rudnick. This manuscript was written by Melissa Scruggs, with revisions and edits from Frank Spera, Matt Rioux, and Wendy Bohrson; visualization and curation of data produced by this study was conducted and maintained by Melissa Scruggs.

DECLARATION OF COMPETING INTERESTS

The authors declare that they have no known competing financial interests or personal relationships that could have appeared to influence the work reported in this paper.

ACKNOWLEDGEMENTS

We would like to thank Roberta Rudnick for her invaluable guidance and insight on many aspects of this project. We would also like to thank Carl Thornber and Michael Garcia for their discussions and communications regarding the nature of this particular eruptive episode, and the National Science Foundation for funding development of the Magma Chamber Simulator (NSF-1551052 to WAB, NSF-0440010 to WAB, and NSF-2151039 to FJS).

DATA AVAILABILITY STATEMENT

Geochemical compositions examined in this study were obtained from Thornber (2001) and Thornber *et al.* (2003a,b). MCS data underlying this article are available in its online supplementary material.

REFERENCES

Bohrson, W.A., Spera, F.J., Ghiorso, M.S., Brown, G.A., Creamer, J.B. & Mayfield, A. (2014). Thermodynamic model for energy-constrained open-system evolution of crustal magma bodies undergoing simultaneous recharge, assimilation, and crystallization: the Magma Chamber Simulator. *Journal of Petrology* 55(9), 1685-1717. doi: 10.1093/petrology/egu036

Bohrson, W.A., Spera, F.J., Heinonen, J.S., Brown, G.A., Scruggs, M.A., Adams, J.V., Zeff, G. & Suikkanen, E. (2020). Diagnosing open-system magmatic processes using the Magma Chamber Simulator (MCS): part I – major elements and phase equilibria. *Contributions to Mineralogy and Petrology* 175, 104. doi: 10.1007/s00410-020-01722-z.

Carmichael, I.S.E. (1991). The redox states of basic and silicic magmas: a reflection of their source regions? *Contributions to Mineralogy and Petrology* 106, 129-141. doi: 10.1007/BF00306429

Clague, D.A. & Dalrymple, G.B. (1987). *The Hawaiian-Emperor Volcanic Chain Part I: Geologic Evolution.* In: Decker, R.W., Wright, T.L. & Stauffer, P.H. (eds.) *Volcanism in Hawaii*. U.S. Geological Survey Professional Paper 1350, Vol. 1, 5-54.

Denlinger, R.P. (1997). A dynamic balance between magma supply and eruption rate at Kilauea volcano, Hawaii. *Journal of Geophysical Research* 102(B8), 18091-18100.

Desmarais, E.K. & Segall, P. (2007). Transient deformation following the 30 January 1997 dike intrusion at Kilauea Volcano, Hawaii. *Bulletin of Volcanology* 69, 353-363. doi: 10.1007/s00445-006-0080-7

Dzurisin, D. & Poland, M.P. (2018). *Magma supply to Kilauea Volcano, Hawaii.* In: Poland, M.P., Garcia, M.O., Camp, V.E. & Grunder, A. (eds) *Field Volcanology: a tribute to the distinguished career of Don Swanson*. Geological Society of America, 275-295.

Edmonds, M., Sides, I. & Maclennan, J. (2015). *Insights into mixing, fractionation, and degassing of primitive melts at Kilauea Volcano, Hawai'i*. In: Heliker, C., Swanson, D.A., & Takahashi, T.J. (eds.) *The Pu'U 'O'o-Kupaianaha Eruption of Kilauea Volcano, Hawai'i: The First 20 Years*. U.S. Geological Survey Professional Paper 1676, 323-350. doi: 10.3133/pp1676.

Gansecki, C., Lee, R.L., Shea, T., Lundblad, S.P., Hon, K. & Parcheta, C. (2019). The tangled tale of Kilauea's 2018 eruption as told by geochemical modeling. *Science* 366, eaaz0147. doi: 10.1126/science.aaz0147.

Garcia, M.O., Pietruszka, A.J., Rhodes, J.M. & Swanson, K. (2000). Magmatic processes during the prolonged Pu'u 'O'o eruption of Kilauea Volcano, Hawaii. *Journal of Petrology* 41(7), 967-990. doi: 10.1093/petrology/41.7.967.

Garcia, M.O., Rhodes, J.M., Trusdell, F.A. & Pietruszka, A.J. (1996). Petrology of lavas from the Puu Oo eruption of Kilauea Volcano: III. The Kupaianaha episode (1986-1992). *Bulletin of Volcanology* 58, 359-379. doi: 10.1007/s004450050145.

Garcia, M.O., Rhodes, J.M., Wolfe, E.W., Ulrich, G.E. & Ho, R.A. (1992). Petrology of lavas from episodes 2-47 of the Puu Oo eruption of Kilauea Volcano, Hawaii: evaluation of magmatic processes. *Bulletin of Volcanology* 55, 1-16. doi: 10.1007/BF00301115.

Geshi, N., Browning, J. & Kusumoto, S. (2020). Magmatic overpressures, volatile exsolution and potential explosivity inferred via dike aspect ratios. *Nature Scientific Reports* 10(9406), doi: 10.1038/s41598-020-66226-z.

Ghiorso, M.S. & Gualda, G.A.R. (2015). An H_2O-CO_2 mixed fluid saturation model compatible with rhyolite-MELTS. *Contributions to Mineralogy & Petrology* 169(53), doi: 10.1007/s00410-015-1141-8.

Gualda, G.A.R., Ghiorso, M.S., Lemons, R.V. & Carley, T.L. (2012). Rhyolite-MELTS: a modified calibration of MELTS optimized for silica-rich, fluid-bearing magmatic systems. *Journal of Petrology*, 53(5) 875-890. doi: 10.1093/petrology/egr080.

Harris, A.J.L., Keszthelyi, L., Flynn, L.P., Mouginis-Mark, P.J., Thornber, C., Kauahikaua, J., Sherrod, D., Trusdell, F., Sawyer, M.W., & Flament, P. (1997). Chronology of the episode 54 eruption at Kilauea Volcano, Hawaii, from GOES-9 satellite data. *Geophysical Research Letters* 24(24), 3281-3284.

Harris, A.J.L. & Thornber, C.R. (1999). Complex effusive events at Kilauea as documented by the GOES satellite and remote video cameras. *Bulletin of Volcanology* 61, 382-395.

Heliker, C. & Mattox, T.N. (2003). *The first two decades of the Pu'u 'O'o-Kupaianaha Eruption: chronology and selected bibliography*. In: Heliker, C., Swanson, D.A., & Takahashi, T.J. (eds.) *The Pu'U 'O'o-Kupaianaha Eruption of Kilauea Volcano, Hawai'i: The First 20 Years*. U.S. Geological Survey Professional Paper 1676, 1-28.

Helz, R.T., Clague, D.A., Sisson, T.W. & Thornber, C.R. (2014). *Petrologic insights into basaltic volcanism at historically active Hawaiian volcanoes*. In: Poland, M.P., Taeko, J.T. & Landowski, C.M. (eds.) *Characteristics of Hawaiian Volcanoes*. U.S. Geological Survey Professional Paper 1801, 237-292.

Jackson, D.B., Swanson, D.A., Koyanagi, R.Y. & Wright, T.L. (1975). *The August and October 1968 East Rift Eruptions of Kilauea Volcano, Hawaii*. U.S. Geological Survey Professional Paper 890, 1-33.

Langmuir, C.H., Vocke, R.D., Jr., Hanson, G.N. & Hart, S.R. (1978). A general mixing equation with applications to Icelandic basalts. *Earth and Planetary Science Letters* 37, 380-392. doi: 10.1016/0012-821X(78)90053-5.

Moore, J.G. & Koyanagi, R.Y. (1969). The October 1963 eruption of Kilauea Volcano Hawaii. U.S. Geological Survey Professional Paper 614-C, 13 p.

Nakata, J., Heliker, C., Sherrod, D. & Thornber, C. (2000). Hawaiian Volcano Observatory summary 97; part 1, seismic data, January to December 1997. U.S. Geological Survey Open-File Report 00-408, 99 p.

Neal, C.A., Brantley, S.R., Antolik, L., Babb, J.L., Burgess, M., Calles, K., Cappos, M., Chang, J.C., Conway, S., Desmither, L., Dotray, P., Elias, T., Fukunaga, P., Fuke, S., Johanson, I.A., Kamibayashi, K., Kauahikaua, J., Lee, R.L., Pekalib, S., Miklius, A., Million, W., Moniz, C.J., Nadeau, P.A., Okubo, P., Parcheta, C., Patrick, M.R., Shiro, B., Swanson, D.A., Tollett, W., Trusdell, F., Younger, E.F., Zoeller, M.H., Montgomery-Brown, E.K., Anderson, K.R., Poland, M.P., Ball, J.L., Bard, J., Coombs, M., Dietterich, H.R., Kern, C., Thelen, W.A., Cervelli, P.F., Orr, T., Houghton, B.F., Gansecki, C., Hazlett, R., Lundgren, P., Diefenbach, A.K., Lerner, A.H., Waite, G., Kelley, P., Clor, L., Werner, C., Mulliken, K., Fisher, G. & Damby, D. (2019). The 2018 rift eruption and summit collapse of Kilauea Volcano. *Science*, 363, 367-374. doi: 10.1126/science.aav7046.

Neall, V.E. & Trewick, S.A. (2008). The age and origin of the Pacific islands: a geological overview. *Philosophical Transactions of the Royal Society B* 363, 3293-3308. doi: 10.1098/rstb.2008.0119.

O'Connor, J.M., Steinberger, B., Regelous, M., Koppers, A.A.P., Wijbrans, J.R., Haase, K.M., Stoffers, P., Jokat, W. & Garbe-Schönberg, D. (2013). Constraints on past plate and mantle motion from new ages for the Hawaiian-Emperor Seamount Chain. *Geochemistry, Geophysics, Geosystems* 14(10), doi: 10.1002/ggge.20267.

Orr, T.R. (2014). The June-July 2007 collapse and refilling of the Pu'u 'O'o Crater, Kilauea Volcano, Hawai'i: U.S. Geological Survey Scientific Investigations Report 2014-5124, 15 p. doi: 10.3133/sir20145124.

Owen, S., Segall, P., Lisowski, M., Miklius, A., Murray, M., Bevis, M., & Foster, J. (2000). January 30, 1997 eruptive event on Kilauea Volcano, Hawaii, as monitored by continuous GPS. *Geophysical Research Letters* 27(17), 2757-2760. doi: 10.1029/1999GL008454.

Poland, M.P., Miklius, A., Johanson, I.A. & Anderson, K.R. (2021). *A decade of geodetic change at Kilauea's Summit – observations, interpretations, and unanswered questions from studies of the 2008-2018 Halema'uma'u eruption*. In: Patrick, M., Orr, T., Swanson, D. & Houghton, B. (eds.) *The 2008-2018 Summit Lava Lake at Kilauea Volcano, Hawai'i*. U.S. Geological Survey Professional Paper 1867, 29 p. doi: 10.3133/pp1867G.

Poland, M.P., Miklius, A. & Montgomery-Brown, E. (2014). *Magma supply, storage, and transport at shield-stage Hawaiian volcanoes*. In: Poland, M.P., Taeko, J.T. & Landowski, C.M. (eds.) *Characteristics of Hawaiian Volcanoes*. U.S. Geological Survey Professional Paper 1801, 179-234.

Poland, M.P., Miklius, A., Sutton, A.J. & Thornber, C.R. (2012). A mantle-driven surge in magma supply to Kilauea Volcano during 2003-2007. *Nature Geoscience* 5, 295-300. doi: 10.1038/ngeo1426.

Putirka, K. (2008). Thermometers and barometers for volcanic systems. *Reviews in Mineralogy and Geochemistry* 69, 61-120. doi: 10.2138/rmg.2008.69.3.

Putirka, K. (2016). Rates and styles of planetary cooling on Earth, Moon, Mars, and Vesta, using new models for oxygen fugacity, ferric-ferrous ratios, olivine-liquid Fe-Mg exchange, and mantle potential temperature. *American Mineralogist* 101, 819-840.

Segall, P. (2019). Magma chambers: what we can, and cannot, learn from volcano geodesy. *Philosophical Transactions of the Royal Society A* 377, 20180158. doi: 10.1098/rsta.2018.0158.

Segall, P., Cervelli, P., Owen, S., Lisowski, M., & Miklius, A. (2001). Constraints on dike propagation from continuous GPS measurements. *Journal of Geophysical Research* 106(B9), 19301-19317. doi: 10.1029/2001JB000229.

Sherrod, D.R., Sinton, J.M., Watkins, S.E., and Brunt, K.M. (2021), Geologic map of the State of Hawai‘i: U.S. Geological Survey Scientific Investigations Map 3143, pamphlet 72 p., 5 sheets, scales 1:100,000 and 1:250,000, https://doi.org/10.3133/sim3143.

Sutton, A.J., Elias, T. & Kauahikaua, J. (2003). *Lava-effusion rates for the Pu'u 'O'o-Kupaianaha eruption derived from* SO_2 *emissions and very low frequency (VLF) measurements*. In: Heliker, C., Swanson, D.A., & Takahashi, T.J. (eds.) *The Pu'U 'O'o-Kupaianaha Eruption of Kilauea Volcano, Hawai'i: The First 20 Years*. U.S. Geological Survey Professional Paper 1676, 137-148.

Thornber, C.R. (2001). Olivine-liquid relations of lava erupted by Kilauea Volcano from 1994 to 1998: Implications for shallow magmatic processes associated with the ongoing East-Rift-Zone eruption. *The Canadian Mineralogist* 39, 239-266. doi: 10.2113/gscanmin.39.2.239.

Thornber, C.R., Heliker, C., Sherrod, D.R., Kauahikaua, J.P., Miklius, A., Okubo, P.G., Trusdell, F.A., Budahn, J.R., Ridley, W.I. & Meeker, G.P. (2003a). Kilauea East Rift Zone magmatism: An Episode 54 perspective. *Journal of Petrology* 44(9), 1525-1559. doi: 10.1093/petrology/egg048.

[dataset]* Thornber, C.R., Hon, K., Heliker, C. & Sherrod, D.A. (2003b). A compilation of whole-rock and glass major-element geochemistry of Kilauea Volcano, Hawai'i, near-vent eruptive products: January 1983 through September 2001. U.S. Geological Survey Open-File Report 03-477, 8 p. doi: 10.3133/ofr03477.

Thornber, C.R., Orr, T.R., Heliker, C. & Hoblitt, R.P. (2015). *Petrologic testament to changes in shallow magma storage and transport during 30+ years of recharge and eruption at Kilauea Volcano, Hawai'i*. In: Carey, R., Cayol, V., Poland, M. & Weis, D. (eds)

Hawaiian Volcanoes: From Source to Surface. Hoboken, NJ: John Wiley & Sons, 147-188. doi: 10.1002/9781118872079.ch8.

von Engelhardt, W. (1989). Remarks on "ratio plots" and "mixing lines". *Geochimica et Cosmochimica Acta* 53, 2443-2444. doi: 10.1016/0016-7037(89)90364-5.

Walker, B.H., Garcia, M.O., & Orr, T.R. (2019). Petrologic insights into rift zone magmatic interactions from the 2011 eruption of Kilauea Volcano, Hawai'i. *Journal of Petrology* 60(11), 2051-2076. doi: 10.1093/petrology/egz064

Walker, G.P.L. (1986). Koolau Dike Complex, Oahu: Intensity and origin of a sheeted-dike complex high in a Hawaiian volcanic edifice. Geology 14, 310-313.

Walker, G.P.L. (1990). Geology and volcanology of the Hawaiian Islands. *Pacific Science*, 44(4) 315-347.

Wallace, P.J. & Anderson, Jr., A.T. (1998). Effects of eruption and lava drainback on the H_2O contents of basaltic magmas at Kilauea Volcano. *Bulletin of Volcanology* 59, 327-344. doi: 10.1007/s004450050195.

Wright, T.L. & Fiske, R.S. (1971). Origin of the differentiated and hybrid lavas of Kilauea Volcano, Hawaii. *Journal of Petrology* 12(1), 1-65.

Wright, T.L., Kinoshita, W.T. & Peck, D.L. (1968). March 1965 eruption of Kilauea Volcano and the formation of Makaopuhi Lava Lake. *Journal of Geophysical Research* 73(10), 3,181-3,205. doi: 10.1029/JB073i010p03181.

Wright, T.L. & Klein, F.W. (2014). Two hundred years of magma transport and storage at Kilauea Volcano, Hawai'i, 1790-2008. U.S. Geological Survey Professional Paper 1806, 240 p. doi: 10.3133/pp1806.

Wright, T.L. & Takahashi, T.J. (1998). Hawaii bibliographic database. *Bulletin of Volcanology* 59, 276-280.

Ye, C., Liu, X., Zhao, D. & Zhao, S. (2022) Robust seismic images of the Hawaiian plume. *Geophysical Research Letters* 49, e2022GL100707. doi: 10.1029/2022GL100707.

LIST OF FIGURE CAPTIONS

Figure 1. Map of Kilauea volcano on the island of Hawai'i (a; after Orr 2014), and map of fissures within Napau Crater (b; modified from Thornber *et al.*, 2015). Brown lavas in panel (a) are lavas of the Pu'U 'O'o eruption erupted between 1983-2011; those displayed in a red hatched pattern are pre-1983 lavas.

Figure 2. Chemical evolution of lavas erupted immediately preceding, during, and after the Episode 54 event. Compositional and mineralogical data from Thornber (2001) and Thornber *et al.* (2003a). Shaded areas note the maximum and minimum extent of chemical variations within different groups of lavas, with the dashed line representing the average composition for that group.

Figure 3. Variations in rates of magma volume accumulation and geodetic baseline measurements at Kilauea's summit caldera (*from Desmarais & Segall, 2007*), and lava effusion rates based on SO_2 emissions (*from Sutton et al., 2003*) for the recovery period following Episode 54 and early Episode 55. Significant events observed as Kilauea's edifice adjusted to the newly emplaced Episode 54 intrusion (*from Desmarais & Segall, 2007*) are noted by dashed vertical lines.

Figure 4. Variations in melt compositions produced by fractional crystallization (FC) models of five candidate low-MgO endmember (arrested dike) compositions. For compositions where ferric-ferrous ratios were determined using wet chemistry techniques (see Table 4), fO_2 relative

to the QFM buffer was calculated using Eqn. 7 of Putirka (2016). Of the five dikes tested, mineral compositions and modal abundances from Episode 54 lavas are best reproduced by FC of Dike N68-4, using the Magma Chamber Simulator (Bohrson *et al.,* 2014, 2020). Mixing lines (l^{mix}) were constructed by linear regression of the mixed mafic endmember (MME) with measured lava compositions from Fissures A-E and Fissure F, respectively. The wt.% MgO for the low-MgO endmember is determined by the intersection between l^{mix} and the LLD on the Al_2O_3 vs. MgO plot, and wt.% MgO along each l^{mix} is denoted by the blue asterisks and associated blue vertical line Uncertainty fields for MELTS models and variations in geologic parameters were calculated for the fractionation model of N68-4, our preferred parental dike composition.

Figure 5. Constructed low-MgO endmember composition (SSR-minimized method) and Episode 54 mixing model results as calculated by linear combination. Note that although the low-MgO endmember compositions do not lie exactly along the liquid line of descent, they are within either analytical, geologic, or model uncertainty, with the exception of K_2O, P_2O_5 and MnO (see Appendix A for further explanation).

Figure 6. Mineral compositions and crystallization temperatures of phases recovered from Episode 54 lavas as reported by Thornber *et al.* (2003a) compared against phases produced by Magma Chamber Simulator (MCS) mixing models. MCS-produced phases present in modeled hybrid lavas are represented by squares; diamonds represent calculated phases of the low-MgO (dike) magma immediately before hybridization. Symbol colors for MCS-produced phases represent the crystallinity of the modeled low-MgO magma at the time of recharge and

hybridization. Minerals recovered from Episode 54 lavas are colored in greyscale according to their likely source, as classified by Thornber *et al.,* (2003a): light gray circles are mineral compositions likely derived from the low-MgO magma body; dark gray circles are mineral compositions likely derived from high-MgO mafic recharge magmas, and medium-gray circles are mineral compositions likely derived from Episode 54 hybrid lavas.

Figure 7; also Animation 1. Cartoon schematic displaying lateral dike propagation in the presence of topographic relief (modified from Geshi *et al.,* 2020). In the case of Episode 54, Fissures A-E "unzipped" downhill, but the eruption concluded uphill with the opening of Fissure F in the western wall of Napau Crater (see also Fig. 1 & Supp. Fig. 2). In our petrogenetic model, a compositionally stratified dike exists so that the lavas erupted from Fissures A-E are produced by mixing between the mixed mafic endmember (MME) magma and a portion of the arrested dike that fractionated ~23% from the initial intrusion composition (similar to the bulk rock composition of N68-4, Jackson *et al.,* 1975). The portions of the dike involved in this mixing event were ~40-50% crystalline at the time of mixing, as constrained by comparison between the mineral compositions and assemblages produced in the MCS models and observed mineral assemblages in erupted lavas. Constructed low-MgO endmember magmas for the Fissure F mixing models are more buoyant (Table 6) than the Fissures A-E low-MgO endmember, and Fissure F opened up-rift at a slightly greater elevation than the previous fissures of this eruptive episode. The low-MgO mixing component necessary to replicate the average bulk composition of Fissure F lavas is derived by mixing of the mixed mafic endmember (MME) magma with a portion of the dike that is ~35% fractionated from the initial intrusion composition (similar to the bulk rock composition of N68-4, Jackson *et al.,* 1975); these upper portions of the dike were

~40-50% crystalline at the time of mixing, as constrained by the mineral assemblages in the MCS models versus the observed mineral assemblages in erupted lavas.

LIST OF TABLES

Figure 1

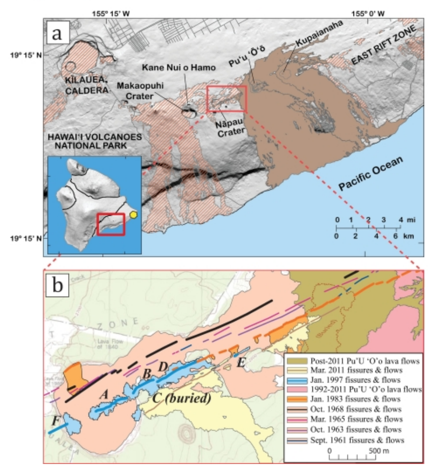

Figure 1. Map of Kilauea volcano on the island of Hawai'i (a; after Orr 2014), and map of fissures within Napau Crater (b; modified from Thornber et al., 2015). Brown lavas in panel (a) are lavas of the Pu'U 'O'o eruption erupted between 1983-2011; those displayed in a red hatched pattern are pre-1983 lavas.

478x426mm (300 x 300 DPI)

Figure 2

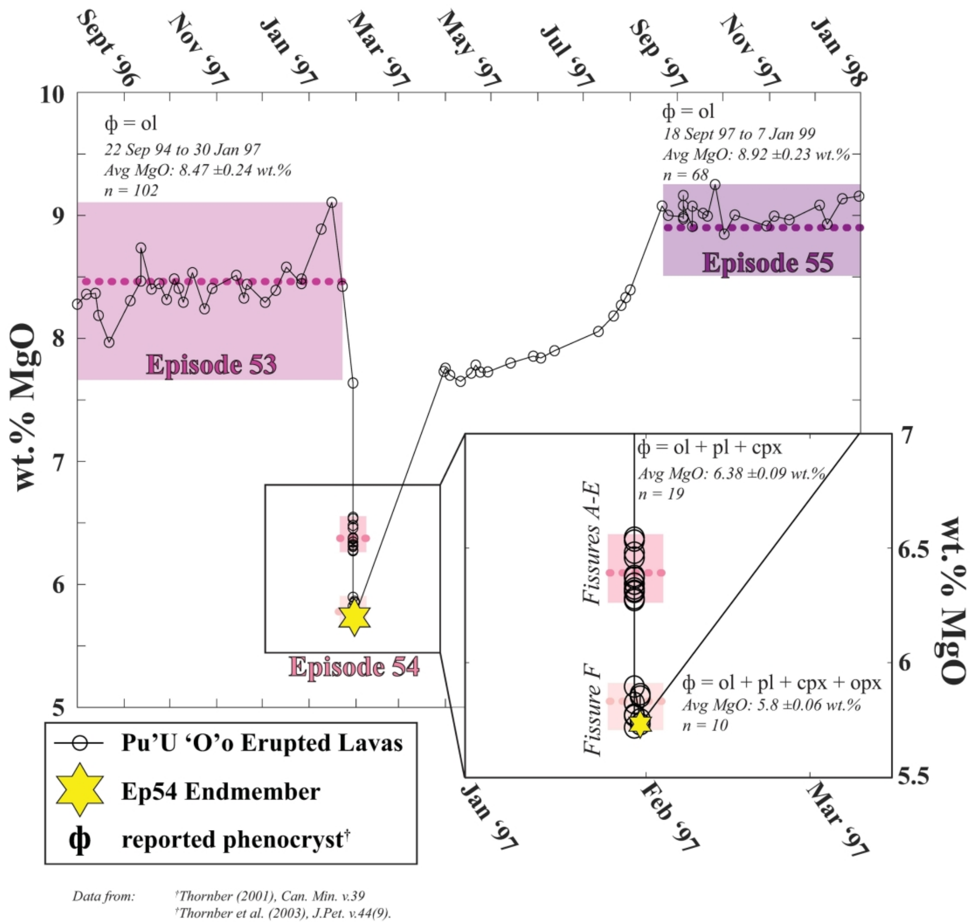

Figure 2. Chemical evolution of lavas erupted immediately preceding, during, and after the Episode 54 event. Compositional and mineralogical data from Thornber (2001) and Thornber et al. (2003a). Shaded areas note the maximum and minimum extent of chemical variations within different groups of lavas, with the dashed line representing the average composition for that group.

248x248mm (300 x 300 DPI)

Figure 3

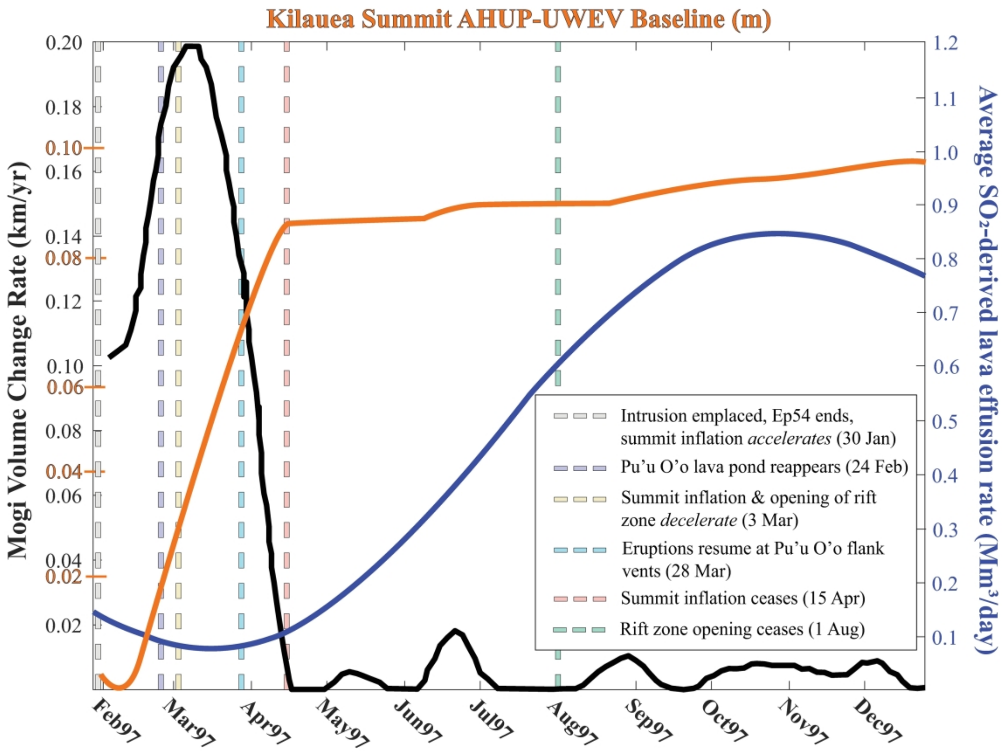

325x262mm (300 x 300 DPI)

Figure 4

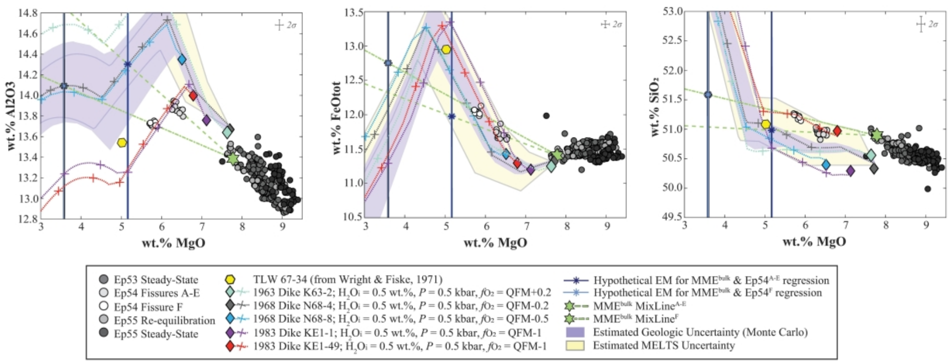

Figure 4. Variations in melt compositions produced by fractional crystallization (FC) models of five candidate low-MgO endmember (arrested dike) compositions. For compositions where ferric-ferrous ratios were determined using wet chemistry techniques (see Table 4), fO2 relative to the QFM buffer was calculated using Eqn. 7 of Putirka (2016). Of the five dikes tested, mineral compositions and modal abundances from Episode 54 lavas are best reproduced by FC of Dike N68-4, using the Magma Chamber Simulator (Bohrson et al., 2014, 2020). Mixing lines (lmix) were constructed by linear regression of the mixed mafic endmember (MME) with measured lava compositions from Fissures A-E and Fissure F, respectively. The wt.% MgO for the low-MgO endmember is determined by the intersection between lmix and the LLD on the Al2O3 vs. MgO plot, and wt.% MgO along each lmix is denoted by the blue asterisks and associated blue vertical line Uncertainty fields for MELTS models and variations in geologic parameters were calculated for the fractionation model of N68-4, our preferred parental dike composition.

371x160mm (300 x 300 DPI)

Supplemental Fig. A1

Figure 5

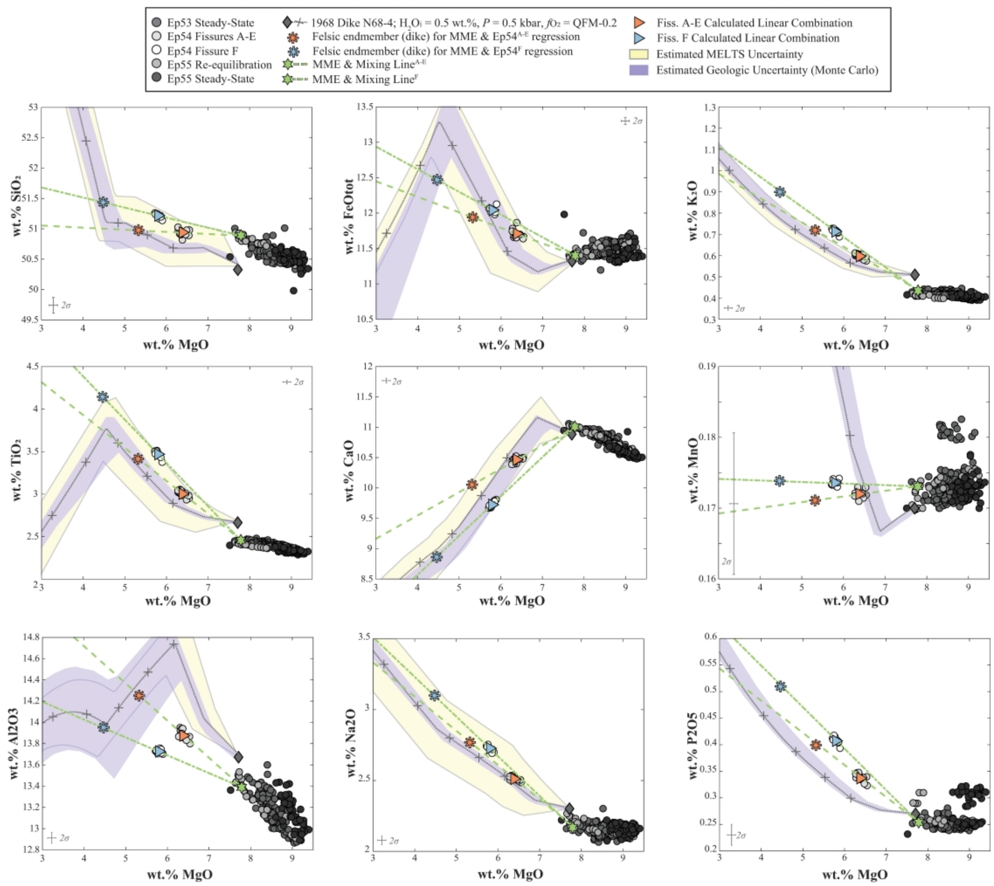

Figure 5. Constructed low-MgO endmember composition (SSR-minimized method) and Episode 54 mixing model results as calculated by linear combination. Note that although the low-MgO endmember compositions do not lie exactly along the liquid line of descent, they are within either analytical, geologic, or model uncertainty, with the exception of K2O, P2O5 and MnO (see Appendix A for further explanation).

359x390mm (600 x 600 DPI)

Figure 6

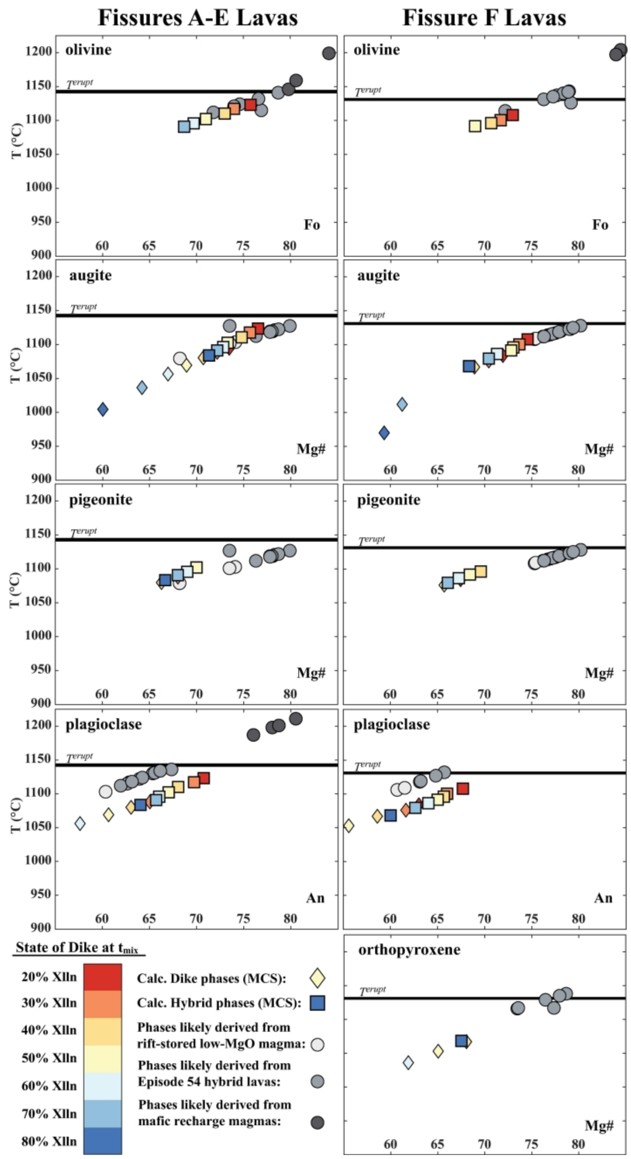

Figure 6. Mineral compositions and crystallization temperatures of phases recovered from Episode 54 lavas as reported by Thornber et al. (2003a) compared against phases produced by Magma Chamber Simulator (MCS) mixing models. MCS-produced phases present in modeled hybrid lavas are represented by squares; diamonds represent calculated phases of the low-MgO (dike) magma immediately before hybridization. Symbol colors for MCS-produced phases represent the crystallinity of the modeled low-MgO magma at the time of recharge and hybridization. Minerals recovered from Episode 54 lavas are colored in greyscale according to their likely source, as classified by Thornber et al., (2003a): light gray circles are mineral compositions likely derived from the low-MgO magma body; dark gray circles are mineral compositions likely derived from high-MgO mafic recharge magmas, and medium-gray circles are mineral compositions likely derived from Episode 54 hybrid lavas.

161x311mm (300 x 300 DPI)

Fig. 7

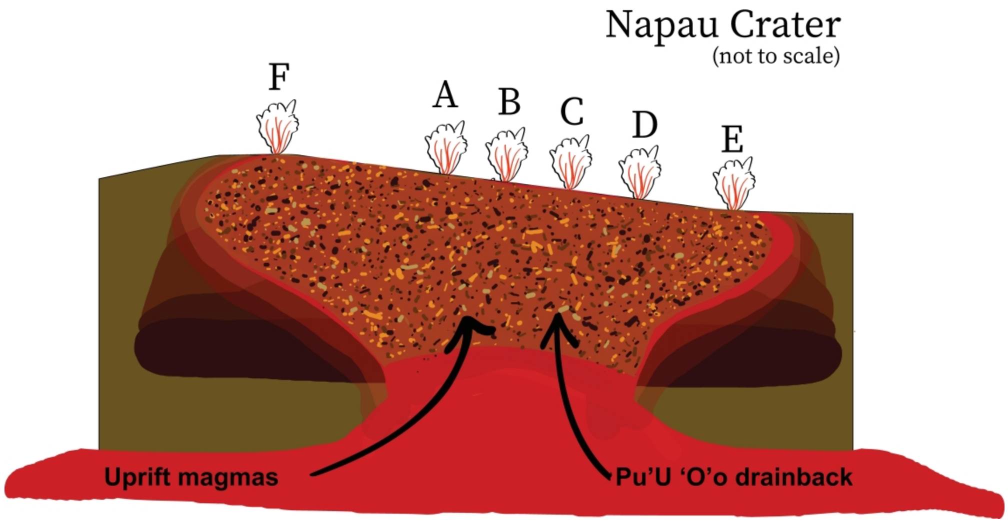

Figure 7; also Animation 1. Cartoon schematic displaying lateral dike propagation in the presence of topographic relief (modified from Geshi et al., 2020). In the case of Episode 54, Fissures A-E "unzipped" downhill, but the eruption concluded uphill with the opening of Fissure F in the western wall of Napau Crater (see also Fig. 1 & Supp. Fig. 2). In our petrogenetic model, a compositionally stratified dike exists so that the lavas erupted from Fissures A-E are produced by mixing between the mixed mafic endmember (MME) magma and a portion of the arrested dike that fractionated ~23% from the initial intrusion composition (similar to the bulk rock composition of N68-4, Jackson et al., 1975). The portions of the dike involved in this mixing event were ~40-50% crystalline at the time of mixing, as constrained by comparison between the mineral compositions and assemblages produced in the MCS models and observed mineral assemblages in erupted lavas. Constructed low-MgO endmember magmas for the Fissure F mixing models are more buoyant (Table 6) than the Fissures A-E low-MgO endmember, and Fissure F opened up-rift at a slightly greater elevation than the previous fissures of this eruptive episode. The low-MgO mixing component necessary to replicate the average bulk composition of Fissure F lavas is derived by mixing of the mixed mafic endmember (MME) magma with a portion of the dike that is ~35% fractionated from the initial intrusion composition (similar to the bulk rock composition of N68-4, Jackson et al., 1975); these upper portions of the dike were ~40-50% crystalline at the time of mixing, as constrained by the mineral assemblages in the MCS models versus the observed mineral assemblages in erupted lavas.

494x279mm (300 x 300 DPI)

Table 1. Input Parameters for the Magma Chamber Simulator (Bohrson *et al*. 2014; Bohrson *et al.* 2020)

Input Parameters for Composite System	
Pressure:	P (bars)
fO_2 constraint	fO_2 buffer or initial Fe^{2+}/Fe^{3+}
Temperature decrement to subsystem M during approach towards T_{end}:	ΔT (°C)
Desired final temperature for end of MCS simulation:	T_{end} (°C)
M subsystem melt temperature for *j*th recharge event:	T_1^M, T_2^M, etc.
Ratio of mass of mafic recharge event to initial mass of rift-stored magma body:	M_j^{MME} / M_0^{Rmagma}

Magma body & Recharge magma subsystem inputs for MCS Simulations

Subsystem	Initial bulk major oxide, trace element, and isotopic composition (for *i* components)	Temperature	Distribution Coefficient	Mass
Magma body (M)	X_0^M	initial T of subsystem T_0^M	D for each component & mineral phase	initial mass of subsystem (100% melt), M_0^M
Recharge, *j* events (R_j)	$X_{0,j}^R$	T_j^R	D for each component & mineral phase	mass of *j*th recharge increment, M_j^R

Table 2. Dike and volume estimates for the Episode 54 intrusive event

[1]Along-strike Dike Length (m):	5,150
[1]Vertical Dike Width (m):	2,240
[1]Horizontal Dike Opening (m):	1.96
[1]Eruptive Volume Episode 54 (Mm^3):	0.30
[1]Calculated Intrusion Volume at Time of Eruption (Mm^3):	**22.91**
[1,3]Contribution from Pu'U 'O'o (Mm^3):	12.70
[1,3]Contribution from Makaopuhi (Mm^3):	1.20
[1,2]Contribution from Kilauea Summit (Mm^3):	1.50
Calculated Volume of low-MgO Magma Body (Mm^3):	**7.51**
[3]Calculated Post-Eruptive Transient Volume Accumulation (Mm^3):	6.58
Final Calculated Intrusion Volume (Mm^3):	**29.49**

[1]*Owen et al. (2000)*
[2]*Desmarais & Segall (2007)*
[3]*Segall et al. (2001)*

Table 3. Estimated Magma Volumes, Supply Rates, and Effusion Rates for early Episode 55

date range		*magma volume (Mm^3)*	*no. of days*	*est. magma supply rate (Mm^3/day)*	*no. of erupting days (w/ pauses)*	*est. effusion rate (Mm^3/day)*
31 Jan-24 Feb:	initial rapid refill of system following Ep54 eruption:	7.30	24.33	0.30		
25 Feb-2 Mar:	additional volume to magmatic system / intrusion:	4.00	8.00	0.50		
3 Mar-28 Mar:	additional volume to magmatic system / intrusion:	18.00	24.00	0.75	1.00	0.14
29 Mar-15 Apr:	additional volume to magmatic system / intrusion:	14.40	18.00	0.80	18.00	0.19
16 Apr-31 Jul:	additional volume to ERZ / magmatic system:	96.30	107.00	0.90	103.61	0.68
1 Aug-31 Dec:	additional volume to ERZ / magmatic system:	98.00	98.00	1.00	98.00	0.90

date range		*magma volume (Mm^3)*	*cumulative "refill" vol. (Mm^3)*	*cumulative intrusion vol. (Mm^3)*	*est. cumulative erupted vol. (Mm^3)*
31 Jan-24 Feb:	initial rapid refill of system following Ep54 eruption:	7.30	7.30		
25 Feb-2 Mar:	additional volume to magmatic system:	1.04	8.34		
	additional volume to Ep54 intrusive body:	2.96		2.96	
3 Mar-28 Mar:	additional volume to magmatic system:	14.57	22.91		0.14
	additional volume to Ep54 intrusive body:	3.29		6.25	
29 Mar-15 Apr:	additional volume to magmatic system:	10.67	33.57		3.55
	additional volume to Ep54 intrusive body:	0.33		6.58	
16 Apr-31 Dec:	additional volume to ERZ / magmatic system:	194.30	69.41		162.00

Table 4. Major oxide compositions used in Episode 54 mixing models

	Kilauea Summit Component[1]	Makaopuhi Crater Component[2]	Pu'U 'O'o Drainback (Bulk Rock)[3]	Mixed Mafic Endmember (P = Bulk)[4]	Rift-Stored Magma (K63-2)[5]	Rift-Stored Magma (N68-4)[6]
SiO_2:	50.61	50.06	51.01	50.9	50.56	50.33
TiO_2:	2.4	2.62	2.44	2.45	2.65	2.66
Al_2O_3:	13.19	13.19	13.43	13.39	13.67	13.67
Fe_2O_3:		1.47			1.73	1.44
FeO:		9.81			9.52	9.88
FeO_{tot}:†	11.5	11.28	11.4	11.4	11.25	11.32
MgO:	8.47	8.49	7.64	7.79	7.64	7.71
MnO:	0.17	0.17	0.17	0.17	0.17	0.17
CaO:	10.83	10.73	11.06	11.01	10.99	10.89
Na_2O:	2.15	2.28	2.16	2.17	2.32	2.3
K_2O:	0.42	0.53	0.43	0.44	0.56	0.51
P_2O_5:	0.26	0.27	0.25	0.25	0.25	0.27
H_2O:‡	0.3	0.2	0.3	0.29	0.06	0.04
CO_2:‡	0.02	0.01	0.02	0.02	0.03	0.02

[1]Episode 53 steady-state average composition, Table 1 in Thornber *et al*. (2003a). Wt.% H_2O & wt.% CO_2 imputed from values given in Mangan *et al.* (2014).

[2]Makaopuhi Crater Pumice M26, erupted 15 March 1965, Table 6 in Wright *et al.* (1968).

[3]Episode 53 KE53-1844, erupted 30 January 1997, in Thornber *et al*. (2003b). Wt.% H_2O & wt.% CO_2 imputed from values given in Mangan *et al.* (2014).

[4]Calculated MME from mixing Components 1-3.

[5]Napau Crater basalt 2, erupted October 1963, in Moore & Koyanagi (1969).

[6]Fissure spatter erupted 13 October 1968, 0.5 km west of Napau Crater; see Table 2 in Jackson *et al.* (1975)

Table 4, cont. Major oxide compositions used in Episode 54 mixing models

	Rift-Stored Magma (N68-8)[7]	Rift-Stored Magma (KE1-1)[8]	Rift-Stored Magma (KE1-49)[8]	Ep 54 Avg Fissures A-E[9]	Ep 54 Avg Fissure F[9]	Ep 55 Mafic Recharge Magma[10]
SiO_2:	50.39	50.3	50.98	50.92	51.2	50.39
TiO_2:	2.91	2.8	2.71	3	3.46	2.31
Al_2O_3:	14.35	13.76	14.04	13.88	13.72	13.05
Fe_2O_3:	1.35					
FeO:	10.08					
FeO_{tot}:[†]	11.43	11.2	11.27	11.7	12.1	11.51
MgO:	6.52	7.13	6.79	6.38	5.8	9.25
MnO:	0.17	0.17	0.17	0.17	0.17	0.17
CaO:	10.74	11.54	10.89	10.46	9.73	10.57
Na_2O:	2.47	2.23	2.35	2.52	2.72	2.1
K_2O:	0.59	0.53	0.52	0.6	0.71	0.39
P_2O_5:	0.28	0.32	0.29	0.36	0.43	0.25
H_2O:[‡]	0.06	0.5	0.5	--	--	0.7
CO_2:[‡]	0.01	0.02	0.02	--	--	0.02

[7]Fissure spatter erupted 14 October 1968 from easternmost eruptive vent; see Table 2 in Jackson *et al.* (1975)

[8]Episode 1 lavas erupted 3 January 1983, in Thornber *et al*. (2003b). Wt.% H_2O & wt.% CO_2 imputed from values given in Wallace & Anderson (1998) and Mangan *et al.* (2014).

[9]Average of Episode 54 Fissure A-E & Fissure F bulk rock compositions, from Thornber *et al*. (2003a).

[10]Episode 55 KE55-1924, erupted September 26, 1997, in Thornber *et al*. (2003b). Wt.% H_2O & wt.% CO_2 imputed from values given in Wallace & Anderson (1998) and Mangan *et al.* (2014).

[†]For compositions where FeO and Fe_2O_3 were not measured using wet chemistry techniques, FeO_{tot} is reported

Table 5. Major oxide compositions of endmember magma compositions and selected input parameters for Episode 54 mixing models

	Mixed Mafic Endmember (MME)[1]	Dike X[2] to match MME & A-E lavas	Dike X[3] to match MME & F lavas
SiO_2:	50.76	50.64	51.03
TiO_2:	2.45	3.39	4.11
Al_2O_3:	13.35	14.14	13.84
$FeO_{tot:}$	11.37	11.86	12.37
MgO:	7.76	5.28	4.43
MnO:	0.17	0.17	0.17
CaO:	10.98	9.99	8.80
Na_2O:	2.16	2.75	3.08
K_2O:	0.43	0.72	0.90
P_2O_5:	0.25	0.40	0.51
H_2O:	0.29	0.65	0.76
CO_2:	0.02	0.02	0.02
% fractionated from initial X:	0.03	23.25 ± 3.25	34.93 ± 5.15
f_{mix} low-MgO:	--	0.57 ± 0.01	0.60 ± 0.00
P (kbar):	--	500	100
M^{MME} / $M^{rift\text{-}stored}$:	--	0.75	0.67
T^M (°C):	1181	--	--
ΔT (°C):	5	--	--
20% Xlln T^R (°C):	--	1096	1084
30% Xlln T^R (°C):	--	1087	1076
40% Xlln T^R (°C):	--	1075	1067
50% Xlln T^R (°C):	--	1057	1053
60% Xlln T^R (°C):	--	1031	1036
70% Xlln T^R (°C):	--	994	1012
80% Xlln T^R (°C):	--	948	970
T_{stop} (°C):	900	900	900

[1]Calculated MME from Table 2 renormalized to 100 wt.% in rhyolite-MELTS v1.1.0, with initial Fe^{2+}:Fe^{3+} set at QFM-1 values.
[2]Best-fit felsic endmember to reproduce Fiss A-E lavas, renormalized to 100 wt.% in rhyolite-MELTS v1.1.0, with initial Fe^{2+}:Fe^{3+} set at QFM values.
[3]Best-fit felsic endmember to reproduce Fiss F lavas, renormalized to 100 wt.% in rhyolite-MELTS v1.1.0, with initial Fe^{2+}:Fe^{3+} set at QFM values.

Table 6a. Mineral assemblages and compositions produced by MCS forward models for Fissure A-E lavas and resultant specific enthalpies for each equilibrated mineral assemblage.

MCS Run	Rift-Stored Magma		Phases Present in Rift-Stored Magma	Fo (ol)	Mg (cpx1)	Mg (cpx2)	An (pl)	Mg (opx)	h_{dike} (J/kg)
	Xllnty	T (°C)							
20JulB	19.64	1094	cpx + pl + mt		72.81		66.00		$-1.214{\cdot}10^7$
20JulC	29.15	1088	2cpx + pl + mt + il + fl		71.68	67.84	65.66		$-1.218{\cdot}10^7$
20JulA	39.42	1080	2cpx + pl + mt + il + fl		70.18	65.70	64.00		$-1.223{\cdot}10^7$
20JulD	49.42	1069	opx + cpx + pl + mt + il + fl		68.97		61.62	67.20	$-1.228{\cdot}10^7$
20JulF	58.83	1056	opx + cpx + pl + mt + il + fl		66.38		59.60	64.02	$-1.232{\cdot}10^7$
20JulG	68.87	1036	opx + cpx + pl + mt + il + ap + fl		63.72		55.56	60.00	$-1.238{\cdot}10^7$
20JulH	78.99	1004	opx + cpx + pl + mt + il + ap + fl		60.18		51.52	55.79	$-1.245{\cdot}10^7$
MCS Run	**Hybrid Lavas**		**Phases Present in Hybrid Lavas**	**Fo (ol)**	**Mg (cpx1)**	**Mg (cpx2)**	**An (pl)**	**Mg (opx)**	h_{hybrid} **(J/kg)**
	Xllnty	**T (°C)**							
20JulB	7.96	1123.13	ol + cpx + pl + fl	75.76	76.52		70.71		$-2.814{\cdot}10^7$
20JulC	12.31	1117.17	ol + cpx + pl + fl	74.00	75.65		69.70		$-2.819{\cdot}10^7$
20JulA	17.11	1110.17	ol + cpx + pl + fl	73.00	74.78		68.00		$-2.826{\cdot}10^7$
20JulD	22.15	1102.20	ol + 2cpx + pl + fl	71.00	73.28	70.00	67.00		$-2.832{\cdot}10^7$
20JulF	27.95	1095.79	ol + 2cpx + pl + mt + fl	69.70	72.81	69.01	66.00		$-2.838{\cdot}10^7$
20JulG	35.71	1090.85	ol + 2cpx + pl + mt + il + fl	68.69	72.17	68.02	65.66		$-2.846{\cdot}10^7$
20JulH	44.50	1083.52	2cpx + pl + mt + il + fl		71.30	66.67	64.00		$-2.856{\cdot}10^7$

Table 6b. Mineral assemblages and compositions produced by MCS forward models for Fissure F lavas and resultant specific enthalpies for each equilibrated mineral assemblage.

MCS Run	Rift-Stored Magma		Phases Present in Rift-Stored Magma	Fo (ol)	Mg (cpx1)	Mg (cpx2)	An (pl)	Mg (opx)	h_{dike} (J/kg)
	Xllnty	T (°C)							
9MarF	19.74	1084	2cpx + pl + mt + il + fl		71.93	67.44	63.00		$-1.207\cdot10^7$
9MarG	30.02	1076	2cpx + pl + mt + il + fl		70.43	65.70	61.62		$-1.212\cdot10^7$
9MarH	38.39	1067	opx + cpx + pl + mt + il + fl		68.91		58.59	68.09	$-1.216\cdot10^7$
9MarD	49.37	1053	opx + cpx + pl + mt + il + fl		66.67		55.56	65.08	$-1.221\cdot10^7$
9MarJ	59.11	1036	opx + cpx + pl + mt + il + fl		63.64		52.53	61.90	$-1.227\cdot10^7$
9MarL	69.82	1012	2cpx + pl + mt + il + ap + fl		61.21	54.60	48.48		$-1.233\cdot10^7$
9MarM	79.99	970	2cpx + pl + mt + il + ap + fl		59.29	50.00	44.33		$-1.241\cdot10^7$
MCS Run	**Hybrid Lavas**		**Phases Present in Hybrid Lavas**	**Fo (ol)**	**Mg (cpx1)**	**Mg (cpx2)**	**An (pl)**	**Mg (opx)**	**h_{hybrid} (J/kg)**
	Xllnty	**T (°C)**							
9MarF	6.44	1107.84	ol + cpx + pl + fl	73.00	74.56		67.68		$-3.010\cdot10^7$
9MarG	11.44	1100.36	ol + cpx + pl + fl	71.72	73.68		66.00		$-3.017\cdot10^7$
9MarH	16.74	1095.93	ol + 2cpx + pl + mt + il + fl	70.71	73.04	69.59	65.66		$-3.029\cdot10^7$
9MarD	24.53	1091.53	ol + 2cpx + pl + mt + il + fl	69.00	72.81	68.42	65.00		$-3.031\cdot10^7$
9MarJ	31.51	1086.28	2cpx + pl + mt + il + fl		71.30	67.25	64.00		$-3.039\cdot10^7$
9MarL	39.61	1079.43	2cpx + pl + mt + il + fl		70.43	66.08	62.63		$-3.048\cdot10^7$
9MarM	49.29	1068.24	opx + cpx + pl + mt + il + fl		68.33		60.00	67.55	$-3.061\cdot10^7$

Table 7. Calculated bulk magma densities for hypothetical felsic endmember compositions at individual state points (P = 0.1 kbar).

Felsic mixing endmember for Fissures A-E (~23% fractionated from initial intrusion)			
Dike Crystallinity (%)	**φ assemblage**	**Dike T (°C)**	**ρ bulk magma (g/cm^3)**
19.64	ol + cpx + pl + mt + fl	1094	2.44
29.15	2cpx + pl + mt + il + fl	1088	2.37
39.42	2cpx + pl + mt + il + fl	1080	2.23
49.42	opx + cpx + pl + mt + il + fl	1069	2.09
58.83	opx + cpx + pl + mt + il + fl	1056	1.96
68.87	opx + cpx + pl + mt + il + fl	1036	1.84
78.99	opx + cpx + pl + mt + il + whit + fl	1004	1.71
Felsic mixing endmember for Fissure F (~35% fractionated from initial intrusion)			
Dike Crystallinity (%)	**φ assemblage**	**Dike T (°C)**	**ρ bulk magma (g/cm^3)**
19.74	2cpx + pl + mt + il + fl	1084	2.22
30.02	2cpx + pl + mt + il + fl	1076	2.06
38.39	opx + cpx + pl + mt + il + fl	1067	1.94
49.37	opx + cpx + pl + mt + il + fl	1053	1.79
59.11	opx + cpx + pl + mt + il + fl	1036	1.67
69.82	2cpx + pl + mt + il + fl	1012	1.56
79.99	2cpx + pl + mt + il + fl	970	1.48